

CHARACTERIZATION OF NOVEL 3D-PRINTED METAL SHIELDING FOR
BRACHYTHERAPY APPLICATORS

by

Kathleen Maiti McGrath

Submitted in partial fulfilment of the requirements
for the degree of Master of Science

at

Dalhousie University

Halifax, Nova Scotia

August 2023

Dalhousie University is located in Mi'kma'ki, the ancestral and unceded territory of the
Mi'kmaq. We are all Treaty people.

Dedication

I dedicate this dissertation to my family and friends who have supported me through this process, and particularly to my mom without whom I wouldn't have been able to complete this work.

Table of Contents

<i>List of Tables</i>	<i>iv</i>
<i>List of Figures</i>	<i>v</i>
<i>Abstract</i>	<i>ix</i>
1. Introduction	1
1.1. Brachytherapy in Gynecological Cancer	1
1.1.1. Brachytherapy	1
1.1.2. Gynecological Applicators	2
1.2. Gynecological Cancers	12
1.3. Dose Calculation	14
1.4. Film use in brachytherapy	20
1.5. 3D printing	23
1.5.1. 3D printing in gynecological brachytherapy	25
1.5.2. Materials in 3D printing.....	32
1.6. Monte Carlo Simulations	35
1.6.1. Egs_brachy	35
2. Methods and Materials	39
2.1. Metal Samples	39
2.2. Custom Solid Water Phantom	41
2.3. Film Set Up	42
2.3.1. Calibration Measurements	42
2.3.2. Parallel Measurements	45
2.3.3. Depth Dose Measurements	50
2.4. Egs_brachy modeling	55
3. Results	58
3.1. Film	58
3.1.1. Calibration Curve.....	58
3.1.2. Planar	59
3.1.3. Data Validation.....	60
3.1.4. Depth Dose	61
3.2. Egs_brachy	63
4. Discussion	66
4.1. Uncertainty Analysis	66
4.2. Planar	67
4.3. Depth Dose	70
5. Conclusion	74
5.1. Summary of work	74
Bibliography	78

List of Tables

Table 1: Energy spectrum of Cs-137, Ir-192, Pd-103 ([15]) I-125, and Cs-131 ([14])....	15
Table 2: Measurements for all provided stainless steel samples from HP.	40
Table 3: Description and value of uncertainties, using the method of Oare et al. The underlined descriptions are values that are the same from Oare et al., as the same conditions were met.	67

List of Figures

Figure 1: Dose distributions for four different dose delivery plans using a single channel cylindrical applicator [6].....	3
Figure 2: Example of the coordinate system used for dosimetry calculations for TG-43 [5].....	4
Figure 3: Dose distributions from a single channel applicator (A) and a multi-channel applicator (B) [9].....	6
Figure 4: Left applicator with a single channel treating the desired area with only dose delivered through the end of the source seed, right applicator with multiple channels treating desired area with dose delivered through the ends and sides of the source seeds .	7
Figure 5: A ring and tandem applicator (left), and an ovoid and tandem applicator (right) [1], [11]	8
Figure 6: A split ring applicator [11]	9
Figure 7: A Vienna applicator (top left), a Venezia applicator (top right), and a MUPIT applicator (bottom) [11][12]	11
Figure 8: Anatomy of the female reproductive system [13].....	14
Figure 9: The relative importance of the Compton effect, photoelectric effect and pair production at different energies and atomic number (Z) of the material [17]	17
Figure 10: Mass energy absorption coefficients for different tissues compared to that of water [21].....	19
Figure 11: Ratio of TG-186 dose calculation and TG-43 dose calculation with different sources [21].....	20
Figure 12: Photo of two pieces of film, with the direction marked with an arrow (for scanning direction) and the name of the measurement.....	22
Figure 13: HP Metal Jet printing process[29].....	25
Figure 14: Custom 3D printed applicators from Sethi et al. Top Left: 3.5 cm diameter applicator with 10 external catheter channels and a central channel, Top Right: 2 cm diameter applicator with 6 external catheter channels and a central catheter channel, Bottom: 2.7 cm diameter segmented cylinder with a central channel	27

Figure 15: 3D printed implant (transparent orange shape) with dwell segments (left) and the computed channels using their algorithm (right) from Garg et al.....	28
Figure 16: Varian applicators and shielding from the Varian gynecologic brachytherapy catalogue [39].....	30
Figure 17: Demonstration of isodose manipulation using shielding and dwell time [33]	30
Figure 18: Theoretical shielded applicator design, shielding in all directions that do not contain the target [30].....	31
Figure 19: The dose profiles of water and all investigated 3D printing materials.....	33
Figure 20: Generic applicator based on TG-186 [30].....	34
Figure 21: Particle tracking using Monte Carlo EGSnrc package egs_chamber a) normal particle transport of an ionization chamber, b) secondary electron tracks in (a), c) transport using cross-section enhancement in a volume around the chamber, d) secondary electron tracks in (c) [49].....	36
Figure 22: Two examples of Monte Carlo simulation (EGSnrc) and treatment planning system (TPS, using TG-43 formalism) dose profiles being compared in water phantoms and in CT phantoms	38
Figure 23: The metal samples (from left to right, top to bottom: 1 mm, 2 mm, 3 mm, 4 mm, 5 mm, 1 mm spare)	41
Figure 24: Metal sample thicknesses (from left to right, top to bottom: 4 mm, 5 mm, 1 mm spare, 1 mm, 2 mm, 3 mm).....	41
Figure 25: The custom water phantom with the hole for the metal samples and the five 1 mm pieces of solid water used to fill the air gaps.....	42
Figure 26: Diagram of the piece of solid water with the catheter cut outs (shown in blue) they were each 2 cm apart and tape was used to secure the catheters when they were placed	43
Figure 27: Graphic of the calibration set up	45
Figure 28: Graphic of the set up where the metal is halfway between the film and the catheters.	47

Figure 29: Graphic of the planar set up where the metal is directly adjacent to the film.	47
Figure 30: Photograph of assembled planar phantom, catheters are blue and inserted into the phantom via the grooves	48
Figure 31: Oncentra view of the planar measurement treatment plan with the calculated dose values in a 2 cm x 2cm square that is 2 cm from the plane of the catheters. The dwell positions are highlighted with red dots along the blue catheters.	49
Figure 32: Treatment delivery system view of the catheters and their dwell positions as well as a visual representation of the dwell weights (larger circles have a longer dwell time than the smaller circles).	50
Figure 33: Graphic of the depth dose set up.	51
Figure 34: Photograph of the assembled depth dose phantom with blue catheters inserted into the base, and the film between the solid water that are stood up above the catheters	52
Figure 35: Oncentra view of the depth dose measurement treatment plan with the calculated dose values along a line perpendicular from the catheters. The dwell position is highlighted with a red dot in the central catheter (blue).	54
Figure 36: Treatment delivery system view of the single dwell position for the depth dose plan.....	55
Figure 37: Graphic of the egs_brachy phantom.....	56
Figure 38: egs_brachy dose reading, showing the anisotropy of the single seed at the center (red arrows) relative to the plane of the metal (white arrow). The maximum value for the colour scale is 500% dose. Since the metal is denser than the surrounding water, it shows a higher dose deposition.....	57
Figure 39: Calibration curves of the film.....	59
Figure 40: Planar percent dose delivered in water, measured using the red calibration channel. The values using the setup with the metal halfway between the catheters and the film are shown with a circle, and the values from the setup where the metal is directly adjacent to the film are shown with a triangle. The error displayed is 7.5% error on the film measurement, detailed in Table 3.....	60
Figure 41: A comparison of different depth dose in water using egs_brachy, film, the Oncentra planning system, and the expected decay of $1/r^2$. Shaded area around the film curve shows the error of the film measurements.	61

Figure 42: The depth dose measured with film using varying thicknesses of metal ranging from 0 mm to 5 mm.	62
Figure 43: The percent difference from water measured using film. The metal thicknesses range from 1 mm to 5 mm. The error from the film measurements is shown as the shaded region.	63
Figure 44: Depth dose measured using egs_brachy simulations. The thickness of metal simulated range from 1 mm to 5 mm.	64
Figure 45: Percent difference measured using egs_brachy simulations. The metal thicknesses range from 1 mm to 5mm.	65
Figure 46: Graphic demonstration of the different path lengths through the metal with multiple source positions, the circled region highlights where these differences lie.	68
Figure 47: Left: dose delivery plan used by Cunha et al., Right: the resulting percent depth dose curves through water and PC-ISO [26]	71
Figure 48: Percent difference from water, including 10 mm thickness of steel, done using egs_brachy	73
Figure 49: Potential workflow outlined in Semeniuk et al.	77

Abstract

Purpose: To characterize 3D-printed stainless steel metal samples in the presence of an Iridium-192 source for organ-at-risk sparing in gynecologic brachytherapy.

Materials and Methods: Samples of 3D-printed stainless steel (5.5 x 5.5 cm², thickness ranging from 1-5 mm) were embedded in a solid water phantom at varying distances from source catheters. An Ir-192 brachytherapy source was passed through the phantom and resulting dose was measured using EBT3 Gafchromic film. Film was first positioned in the sagittal plane 2 cm away from the catheters, with the metal directly below the film and then with the metal halfway between the film and the catheter (1 cm separation). A plan was created and delivered to give a uniform dose at the film plane. The second setup allowed for measurement of a depth dose curve in solid water by positioning the film in the transverse plane directly above the metal samples. The second setup was recreated using Monte Carlo simulations, using the EGSnrc package `egs_brachy`. The measurements without metal present were used to validate the data between the film and simulation.

Results: The planar dose passing through the metal samples, thickness 1 mm - 5 mm, decreased compared to solid water by $7.4 \pm 6.9\%$, $10.7 \pm 6.7\%$, $15.9 \pm 6.3\%$, $18.8 \pm 6.1\%$, and $26.5 \pm 5.5\%$ respectively. These were measured with the metal midway between the film and the catheter plane. Dose enhancement on the order of 5% was noted when metal was directly adjacent to the film. The average decrease in depth dose from a single dwell position measured using film ranged from $10.0 \pm 5.9\%$ (1 mm) to $21.1 \pm 5.3\%$ (5 mm). The average decrease in depth dose from a single dwell position measured using MC simulation ranged from $3.8 \pm 0.9\%$ (1 mm) to $16.3 \pm 0.9\%$ (5 mm). The depth dose values were measured using a line width of 2.5 mm averaged for film (7 pixels), and 3 mm averaged for MC simulation (3 pixels). The MC simulation and film measurements generally agree within standard error.

Conclusions: The 3D-printed metal samples show potential for use in 3D-printed personalized shielding. A maximum reduction in dose of $26.5 \pm 5.5\%$ compared to solid water was measured 2 cm from the source using the 5 mm sample. An outer layer of solid water can reduce dose enhancement due to increased scatter near the metal. Greater thicknesses would be needed for further dose reduction to OARs and will be investigated in future work

1. Introduction

1.1. Brachytherapy in Gynecological Cancer

1.1.1. Brachytherapy

Brachytherapy is used for treating localized cancers and is limited to tumours of a small size (less than 3 to 4 cm) [1]. The treatment is done using a radioactive isotope that is safely inserted into the patient, either via needles and catheters for interstitial brachytherapy, or by using an applicator designed to be used in an existing body cavity (such as the vagina) for intracavitary brachytherapy. There is also a technique where seeds made of the radioactive isotope are inserted into the patient permanently, for continuous low dose treatment.

Low dose-rate (LDR) brachytherapy uses a source with a dose rate between 0.4 Gy/hr to 2 Gy/hr [1]. High dose-rate (HDR) brachytherapy uses a source with a dose rate of 12 Gy/hr or higher [1]. HDR brachytherapy allows for high doses of radiation to be delivered over several fractions of 10-20 minutes and allows for outpatient treatment instead of hospitalisation, which is required for low dose-rate brachytherapy treatments.

Brachytherapy has historically been used to treat several different cancers (Cervical, vulvar, endometrial, vaginal, uterine, prostate, anal etc.) [1]–[3].

Brachytherapy can be used as the primary treatment method but it is also used in conjunction with surgery, chemotherapy, and external beam radiation treatments [1]–[3]. For intracavitary treatments of gynecological cancers, applicators are used to facilitate the treatment process and achieve the desired dose distribution.

1.1.2. Gynecological Applicators

The single channel cylindrical applicator (also called a cylinder or a vault applicator) is used for vaginal HDR brachytherapy treatment [4]. It is simple and can be used quickly while also being CT and MRI compatible, enabling imaging with applicators in place ahead of treatment [4]. Cylindrical applicators available on the market come in different diameters to account for variations in patient sizing [4]. The cylindrical applicator allows for a radially symmetrical dose to be delivered, which means the treatment plan optimization options are limited [4]. The dose cannot be lowered at a specific point without lowering the dose in an entire radial slice through the applicator (Figure 1). The dose distribution can only be modulated along the length equally on all sides. There can also be some heterogeneity in the dose distribution at the vaginal apex (dose delivered through the tip of the applicator) due to source anisotropy [4]. Source anisotropy is the particular way the shape of a source causes the dose distribution to change from a perfect circle at the ends of the source. Less dose is delivered through the ends of the source [5]. This anisotropy results in as much as a 30% decrease in dose delivered to the vaginal apex [4].

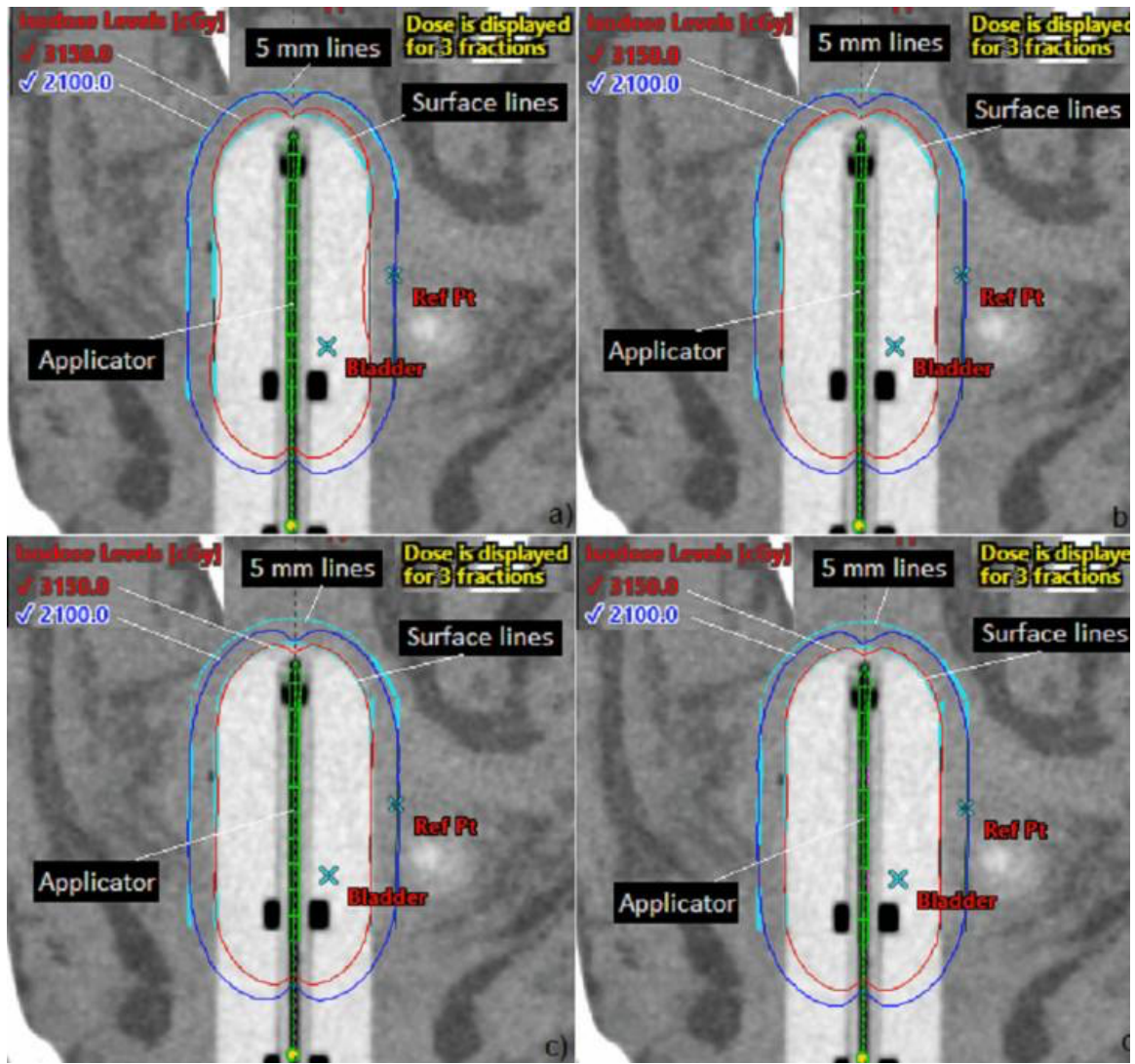


Figure 1: Dose distributions for four different dose delivery plans using a single channel cylindrical applicator [6]

The anisotropy is caused by the shape of the source [5]. As shown in Figure 2, for dose calculations the length and edges of the source seed must be considered [5]. Perpendicular to the long edge of the seed, the distances are relatively similar from both ends of the seed, so the dose does not vary greatly, but looking at the area beyond the ends of the seed (along the z-axis in Figure 2) the distance from the far end is much higher to the point [5]. Due to the inverse

square nature of the radiation strength along a distance, the dose delivered along the z-axis near the source will be lower than the dose delivered to a point of similar distance positioned perpendicular to the long edge of the source [5]. There are also cylindrical applicators that have multiple channels, used to treat vaginal cancer [4]. Using an applicator that has multiple channels allows for the dose to the vaginal apex to be delivered from the seeds through angles that are not directly through the end of the source [7], [8].

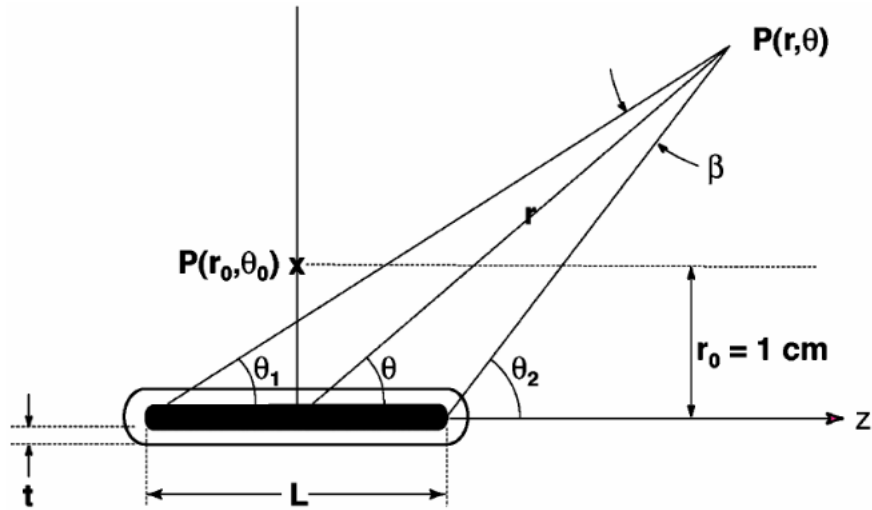


Figure 2: Example of the coordinate system used for dosimetry calculations for TG-43 [5]

With more than one channel available, the dose distribution can be modified in ways that allow for it to be asymmetrical [4]. It has been shown that the inclusion of multiple channels allows for better isodose shaping and control when compared to a single channel applicator, resulting in lower dose to nearby organs at risk while maintaining or improving dose coverage to the CTV (Figure 3) [4]. Reducing dose to nearby organs at risk is particularly beneficial for

patients undergoing re-treatment (post external beam or brachytherapy treatment) and those who may have contraindications (such as diabetes, pelvic inflammatory disease, hypertension, collagen disease, inflammatory bowel disease, or adnexal masses) [1]. This format also corrects the anisotropy at the vaginal apex that is seen in a single channel cylindrical applicator (Figure 4) [4]. The multichannel applicators are available with a range of catheter channels and targeted treatment areas, which can result in improved dose distribution when used for treatment over the single channel applicator [4]. The improvements in dose distribution come at the cost of a more complicated treatment plan and typically increased treatment times when compared to the single channel. The choice between the two applicators is simplicity and speed or increased dose control and complexity.

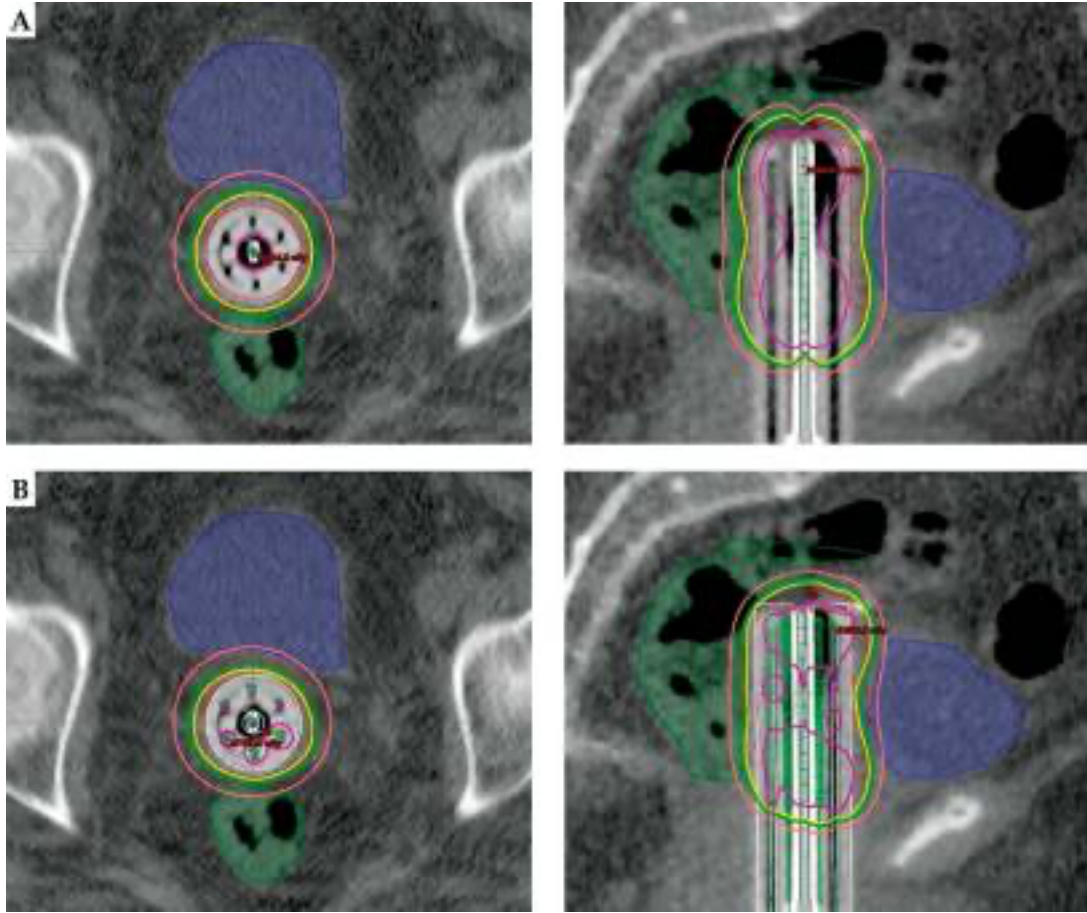


Figure 3: Dose distributions from a single channel applicator (A) and a multi-channel applicator (B) [9]

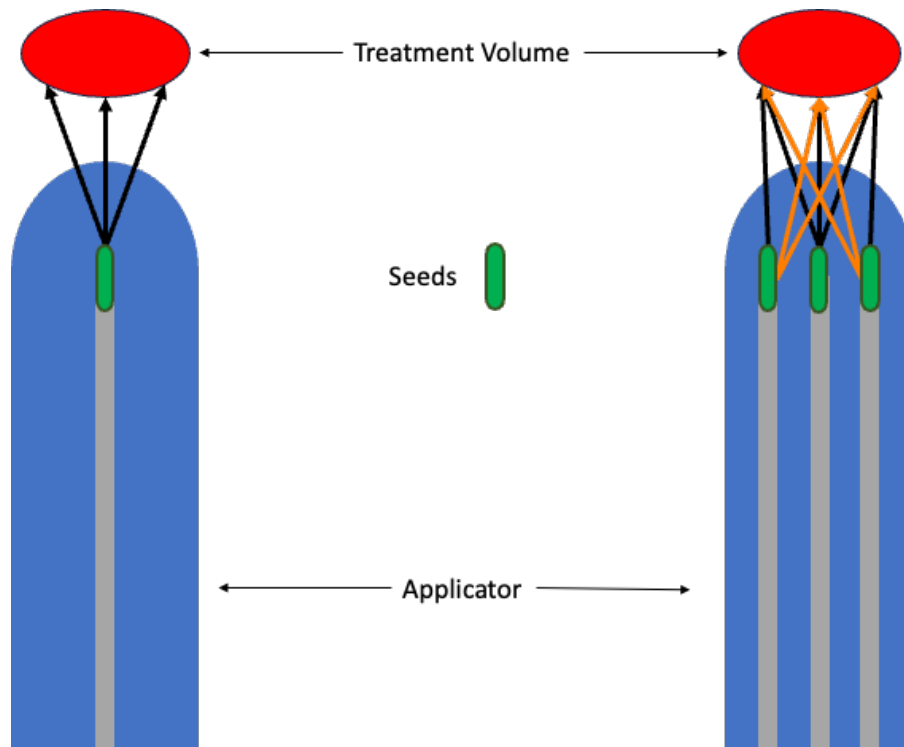


Figure 4: Left applicator with a single channel treating the desired area with only dose delivered through the end of the source seed, right applicator with multiple channels treating desired area with dose delivered through the ends and sides of the source seeds

Another type of applicator is the ring and tandem (R&T) and the ovoid and tandem (O&T) applicators. These applicators can be used interchangeably for treatment and the choice between them typically comes down to anatomy and which applicator will provide a more accurate fit for the patient [10]. The tandem is a central channel and a certain portion of it is inserted into the uterus, through the cervix [11]. The differences between these two applicators come from the ring and ovoid portion of the applicator. The tandem is located at the center of the ring, and the ring itself can guide the radioactive seed around the tandem providing additional dose to chosen areas [11]. The ovoids are smaller cylinders located at either side of the tandem, and the distance between them can be

adjusted if desired [11]. The O&T system has a few different designs, such as the Fletcher and the Henschke applicators [11]. The benefit of the R&T applicator is that the ring is fixed, so the geometry is very easy to reproduce. This can, however, create difficulties with insertion [10], [11]. The R&T can also accommodate source positions around the entire circumference, where the O&T is limited to the ovoid positions to the side [10]. The O&T applicators are best used for patients who have asymmetrical or narrow anatomy [10].

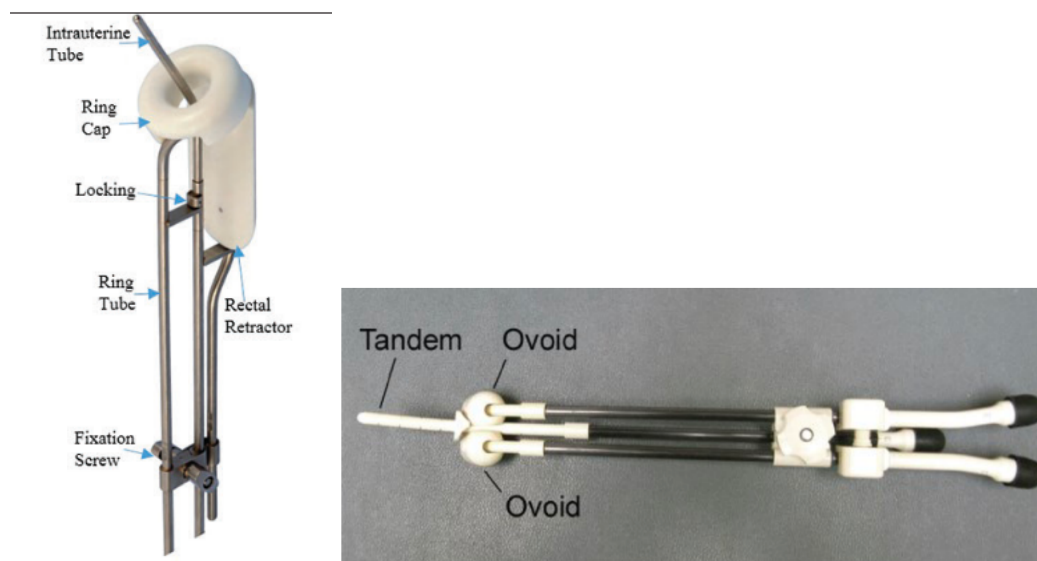


Figure 5: A ring and tandem applicator (left), and an ovoid and tandem applicator (right) [1], [11]

The split ring applicator is similar to the R&T applicator, except the ring can be separated and the diameter changed to better fit patient anatomy [11]. The insertion of this applicator is also easier than with a R&T applicator, as the two ring segments can be inserted separately and the spacing can be adjusted once inside the patient [11]. While this negates the R&T advantage of fixed geometry,

it allows for more flexibility with geometry and dose distribution inside the patient.

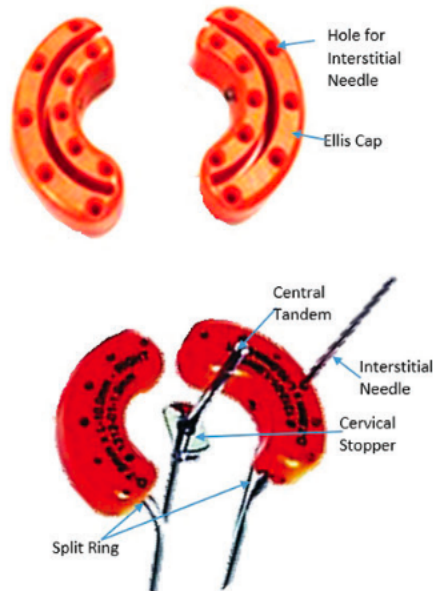


Figure 6: A split ring applicator [11]

There are also some applicators that are used as templates for interstitial brachytherapy or as a combination intracavitary and interstitial system. The Vienna applicator looks like a R&T applicator but the ring also has several holes to guide interstitial needles [11]. The use of needles allows for precise placement and asymmetrical isodose distributions to be achieved for treatment [11]. The Venezia applicator is a hybrid intracavitary/interstitial applicator that uses an O&T style applicator where the ovoids have holes to guide interstitial needles [11]. A perineal interstitial template may also be attached for perineal interstitial needles [11]. The MUPIT (Martinez Universal Perineal Interstitial Template) is a multi-site template for intracavitary/interstitial treatment [11]. It has three large holes for a foley catheter, a vaginal obturator, and a rectum obturator. The rest is a

large interstitial template with spaces for guiding needles [11]. It has holes that allow for perpendicular needles as well as angled needles to achieve the desired dose distribution [11]. The treatment planning for this applicator is complicated by the metal present [11]. Planning images may have artifacts or shadows that obscure the image because of the density of the metal [11].

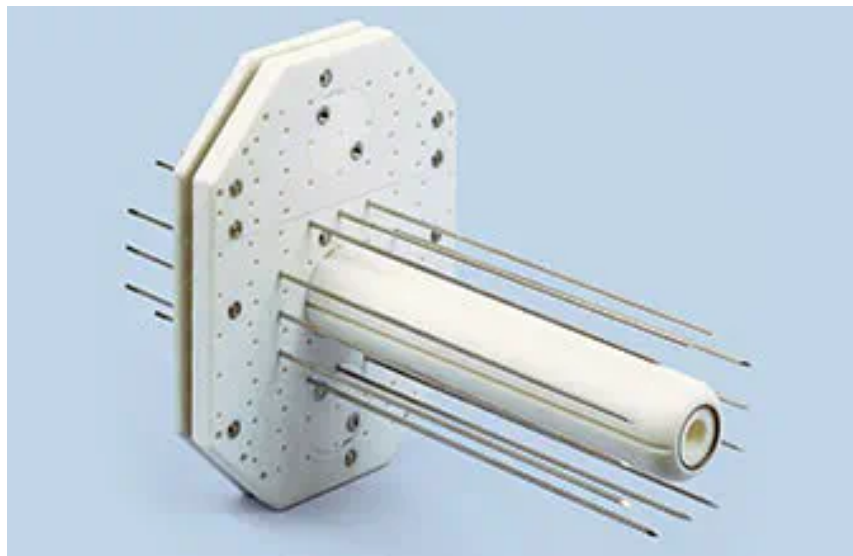
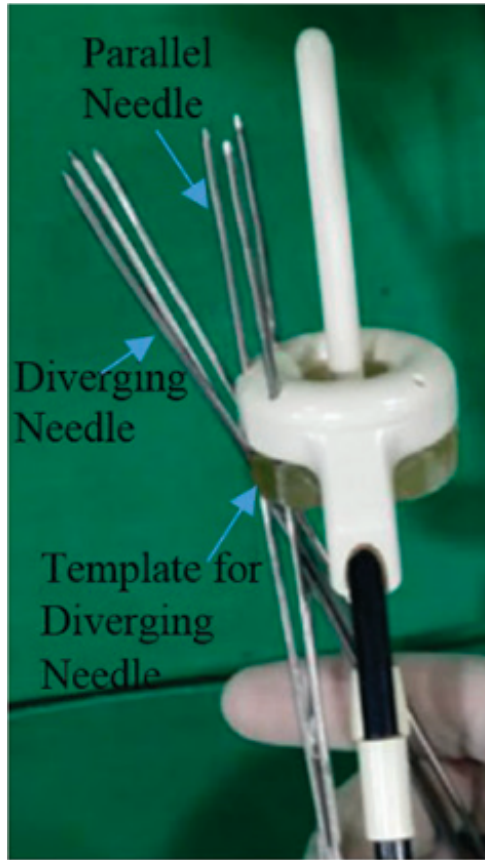


Figure 7: A Vienna applicator (top left), a Venezia applicator (top right), and a MUPIT applicator (bottom) [11], [12]

1.2. Gynecological Cancers

Cancer can occur in all areas of the female reproductive system. Some are treated with surgery, chemotherapy, external beam radiation, brachytherapy or a combination of any of those treatments. Some gynecological cancers are not, or are rarely, treated with radiation (fallopian tube cancer, ovarian cancer) [3].

The type of cell that becomes cancer determines the pathology of the cancer that develops. Vaginal cancer originates in the cells of the vagina [3]. The cancer can be in the cells of the lining of the vagina (squamous cell carcinoma), or in the cells from the glands that make mucus (adenocarcinoma of the vagina) [3]. These two are the most common, but other types of cancer can develop such as melanoma, which affects the pigment cells of the vagina or sarcoma, which affects the muscle or connective tissue of the vagina [3]. Surgery and radiation are both treatment options suggested for most stages, but radiation is suggested for advanced disease [1]. A combination external beam and brachytherapy are used for treatment, and at early stages brachytherapy alone has been able to treat smaller lesions [1].

Cervical cancer originates in the cells of the cervix. The most common cervical cancer is squamous cell carcinoma of the cervix [3]. Cancer in the passageway that connects the uterus to the vagina is in the glandular cells (adenocarcinoma of the cervix) and is less common than cancer in the squamous cells. It is, however, more common than the rare types of cervical cancer such as adenosquamous carcinoma, glassy cell carcinoma, and mucoepidermoid carcinoma. [3]. This cancer is treated with surgery and chemoradiation, the stage

of the disease being the primary factor when deciding between treatment options [1]. Radiation treatment can be delivered with an external beam or via brachytherapy using an applicator with a tandem for targeted cervical treatment [1].

Uterine cancer is the most common gynecological cancer [3]. It originates from the cells of the uterus; most cases are endometrial carcinoma (cancer of the lining of the uterus) [3]. A uterine sarcoma is a cancer that originates in tissues other than the lining, and a third form of uterine cancer, carcinosarcomas, has both carcinomas and sarcomas present [3]. The suggested method of treatment for uterine cancer is to have it surgically removed via hysterectomy [1]. The surgical removal of nearby tissue is determined by the extent of the disease [1]. Since there are lymph nodes nearby to the uterus the removal of lymph nodes is common [1]. Radiation treatment for uterine cancer is rarely chosen as the primary treatment method, it is typically chosen as an adjuvant treatment alongside the primary treatment method [1]. It is used to increase the local control of the tumour in the area of treatment [1].

Vulvar cancer, cancer that originates in the vulva, is typically squamous cell carcinoma, but can also originate in the pigment-making cells as vulvar melanoma [3]. For vulvar melanoma the preferred treatment method is surgery where adjuvant radiation therapy may be considered to reduce the risk of recurrence [1]. Surgery is also the preferred method of treatment for vulvar carcinoma and can be accompanied by chemotherapy and radiation to prevent recurrence after surgery and to shrink the cancer before surgery [1].

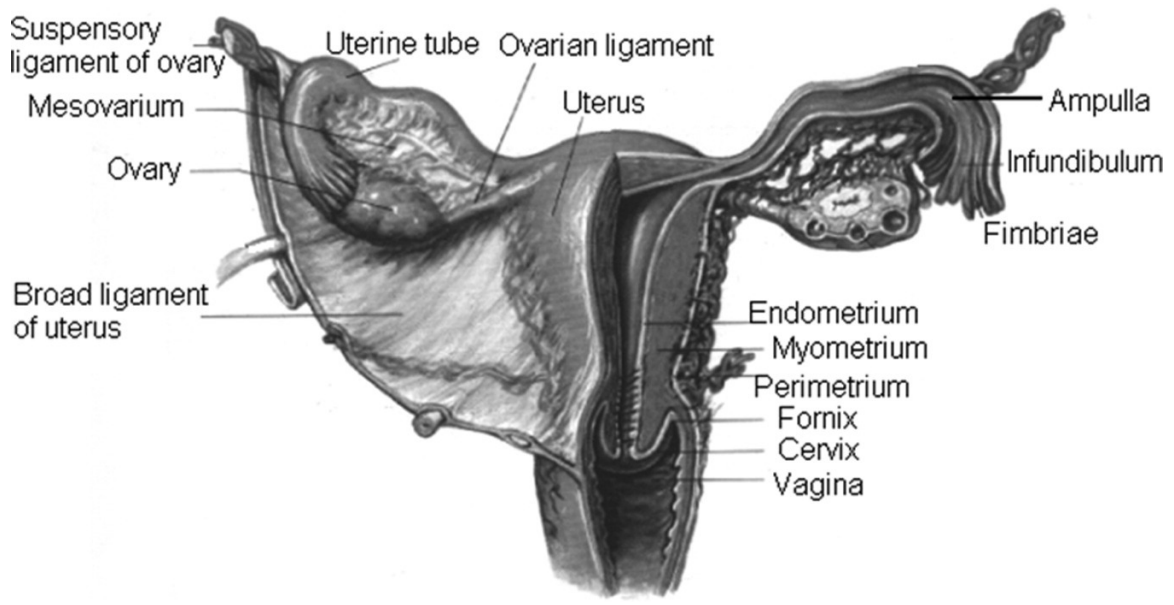


Figure 8: Anatomy of the female reproductive system [13]

1.3. Dose Calculation

There are a number of different radionuclides used as sources for brachytherapy treatment. Sources differ in terms of half-life, specific activity and energy. Some common sources are I-125 (60 day half-life), Pd-103 (17 day half-life), Cs-131 (9.7 day half-life), Cs-137 (30 year half-life), Ir-192 (73.8 day half-life), and Co-60 (5.26 year half-life) [14]–[16]. The energy spectra are shown below in Table 1 and the spectrum for Co-60 has energies of 1.33 MeV and 1.17 MeV each with a probability of 50% [15]. The energy of a source will determine penetration within tissue as well as shielding needs for a brachytherapy treatment room, while the half-life will dictate the frequency with which sources must be replaced. A source with a high specific activity will allow for miniaturization, essential for HDR applications.

Table 1: Energy spectrum of Cs-137, Ir-192, Pd-103 ([15]) I-125, and Cs-131 ([14]).

Cs-137		Ir-192		Pd-103		I-125		Cs-131	
Energy (keV)	Intensity (%)								
4.47	0.914	9.44	3.9216	2.7	8.7321	27.202	0.406	4.11	8.6
31.817	1.995	65.122	2.626	20.074	22.47	27.472	0.757	29.461	21.1
32.194	3.641	66.831	4.441	20.216	42.512	30.98	0.202	29.782	38.9
36.304	0.3489	75.368	0.53111	22.699	3.541	31.71	0.0439	33.562	3.63
36.378	0.67218	75.749	1.02122	22.724	6.8519	35.492	0.0668	33.624	7.02
37.255	0.2136	77.831	0.3648	23.172	1.645			34.419	2.13
283.51	0.00059	136.393	0.19925	39.7488	0.0683				
661.6573	85.102	176.984	0.00431	53.291	3.0E-05				
		280.2724	0.0084	62.413	0.001044				
		295.9565	28.72	241.885	5.0E-07				
		308.45507	29.707	294.9815	0.002807				
		316.50618	82.86	317.725	1.5E-05				
		416.46887	0.67021	357.458	0.02217				
		468.06885	47.843	443.795	1.5E-05				
		485.456	0.00474	497.0801	0.003961				
		588.58107	4.5221						
		593.6319	0.04201						
		599.4115	0.003917						
		604.41105	8.21619						
		612.46215	5.347						
		765.83	0.00136						
		884.53657	0.2927						
		1061.494	0.05316						
		1089.9626	0.0011616						
		1378.5024	0.0014019						

There are five types of high energy photon interactions with matter: the Compton effect, the photoelectric effect, pair production, Rayleigh (coherent) scattering, and photonuclear interactions. Photonuclear interactions do not occur at the energy range of the common brachytherapy sources, these interactions require a photon of at least a few MeV [17]. Rayleigh scattering is present at all energies but is more prominent at lower energies [17]. Rayleigh scattering is an interaction that causes a photon to change direction after interaction with an atom, but no energy is exchanged so this interaction does not contribute to dose [17]. Pair production occurs when a photon is transformed into a positron and electron pair which requires the photon have a minimum energy of 1.022 MeV, the equivalent energy of an electron and a positron [17]. The only common brachytherapy source where pair production could occur is Co-60, or very rarely it could occur with Ir-192 as well (0.0014019%) [15].

The photoelectric effect and Compton effect are dominant in the energy range for brachytherapy [17]. Compton interactions are caused by a photon colliding with a free electron and imparting energy to the electron causing it to move [17]. The photoelectric effect is caused by a photon interacting with an atom and transferring all of its energy to a tightly bound electron, which is then ejected from the atom [17]. The photoelectric effect is dominant at low energies and in intermediate energies where the atomic number of the material is high [17]. The Compton effect is dominant at intermediate energies [17]. The results of a Compton interaction are an electron with an increased kinetic energy, and a scattered photon of decreased energy [17]. The results of a photoelectric interaction are an electron that has escaped an

atom, and an atom that takes the recoil energy [17]. These electrons are ultimately what deposits the energy into the tissue, known as dose deposition [17]. Based on the specific isotope and source geometry used, the likelihood of interactions, and the range and direction of resultant electrons, the overall energy deposited in tissue can be calculated and a full characterization of the dose distribution can be produced.

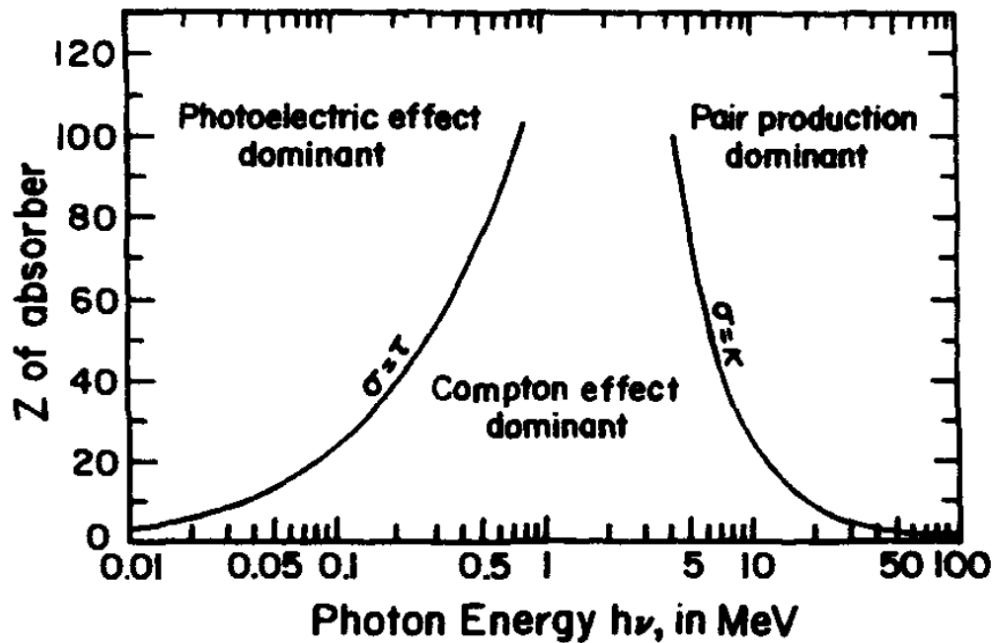


Figure 9: The relative importance of the Compton effect, photoelectric effect and pair production at different energies and atomic number (Z) of the material [17]

The accepted standard for brachytherapy dose calculations is the American Association of Physicists in Medicine (AAPM) Task Group 43 (TG-43) report from 1995. An update was first published in 2004 and additional supplements were posted in 2007 and 2017 [5], [18], [19]. The goal of TG-43 was to formalise a new brachytherapy dose calculation protocol [5]. Previous to the original protocol, calculations were based on apparent activity of a source, the

equivalent mass of radium, exposure-rate constants, and tissue-attenuation coefficients. The methodology did not account for differences that exist between sources [5]. TG-43 used parameters that depended on the specific source and vendor design, which were measured directly or calculated for each seed design [5]. TG-43 improved the standardization of dose calculation methods and well as the dose-rate distributions used for clinical treatment [5]. The difference was as large as 17% between previous dose-rate distributions and the new TG-43 recommended distributions [5]. Most treatment planning software uses TG-43 formalism and the recommended dosimetry parameters [5]. This formalism is used worldwide as the standard for low energy photon emitting brachytherapy and has been widely adopted for HDR treatment planning using an Ir-192 source [20].

TG-186 is the methodology published by AAPM for model-based dose calculation algorithms (MBDCAs) in brachytherapy [20]. It is an advancement in dose calculation; the previous method using TG-43 used a superposition method with precalculated dose distributions from a single seed through water [20]. The method of using MBDCAs allows for calculations of dose through materials other than water, which creates a more accurate dose distribution to what is delivered to the patient (Figure 10) [20]. As other means of treatment improve their standard or practice, it follows that those improvements should be modified for other treatment methods. External beam radiation therapy transitioned to using material heterogeneity corrections as a result of MBDCAs for that treatment modality [20]. When TG-186 was published in 2012, the use of material heterogeneity in dose calculations was not widely used, which TG-186 sought to amend (Figure 11)

[20]. When comparing TG-43 dose calculations to Monte Carlo dose calculations using Ir-192 as a source, they did not agree over the whole area [20]. An overestimation of 13% dose to the spinal cord and an underestimation of 15% to the sternum were found for an esophageal brachytherapy treatment [20]. In a breast treatment, the calculated doses to the volume intended to be treated (planning target volume, PTV) agreed, but the surrounding tissue showed disagreement (TG-43-calculated doses were up to 5% larger for skin dose, and up to 10% larger for lung dose) [20]. A simulation was run with TG-43 conditions (assuming all tissue was water) and with CT scan material values using a shielded endorectal applicator [20]. Small differences were found in the soft tissue, less than 2%, but the differences in more dense material were larger (18%-23% in cortical bone, 5%-7% in femoral bone, and 3%-3.5% in spongiosa) [20].

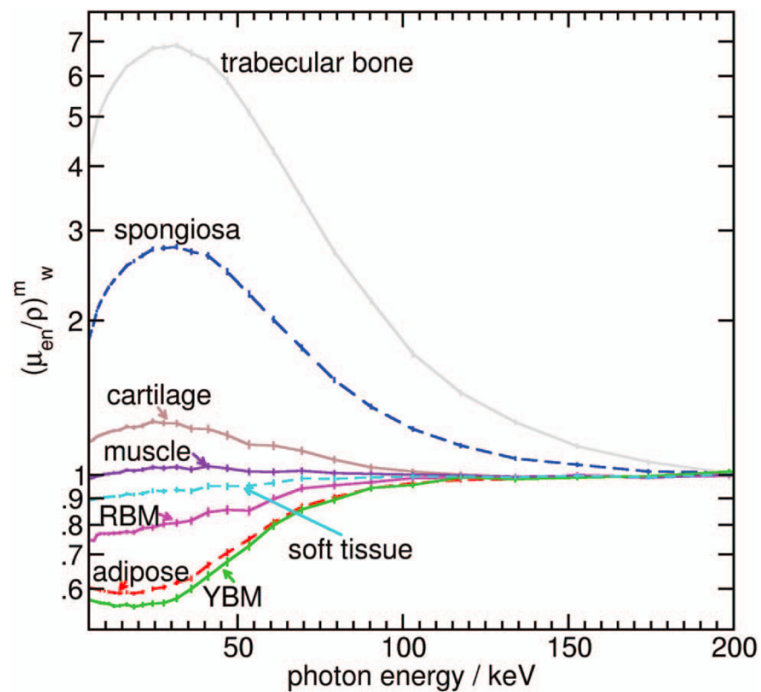


Figure 10: Mass energy absorption coefficients for different tissues compared to that of water [21]

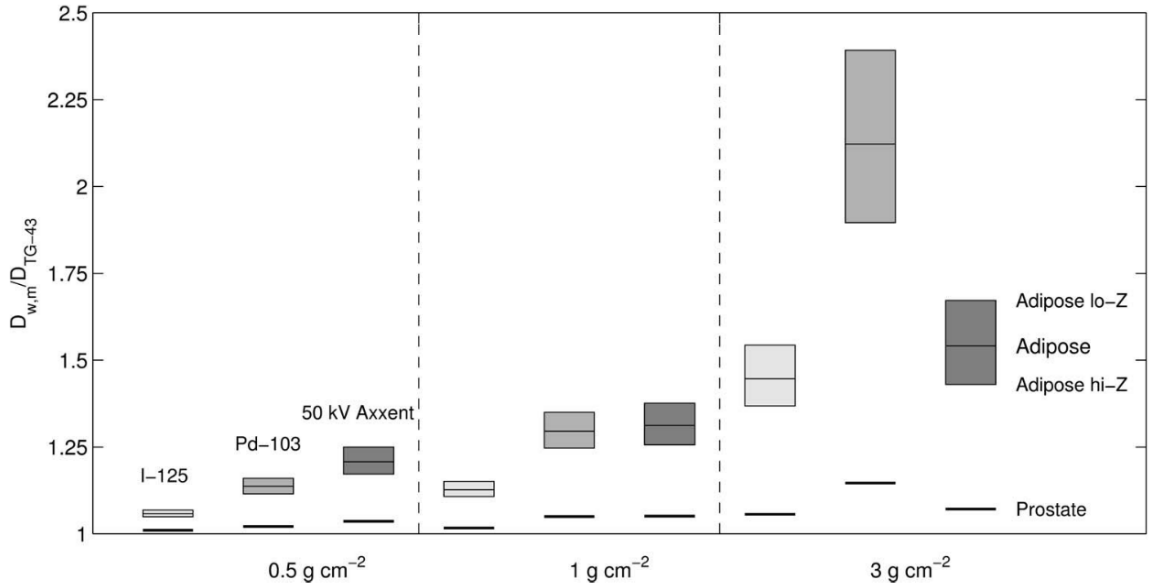


Figure 11: Ratio of TG-186 dose calculation and TG-43 dose calculation with different sources [21]

1.4. Film use in brachytherapy

Radiochromic film is used in brachytherapy as a method for dosimetry with benefits such as high spatial resolution, low energy dependence, and near water equivalence [22]. GAFChromic film (Ashland, Wilmington, Delaware) is a prevalent brand of radiochromic film, and its most recent film design is the EBT3 [22]. The structure of the film is an active layer between two plastic bases [23]. The active layer is 28 μm and contains the active component, a marker dye, stabilizers, and other components which allow the film to be nearly energy-independent [23]. The thickness of the active layer will vary slightly between different productions lots, which will result in slightly different pixel colour values between lots [23]. The base pieces are 125 μm of clear polyester substrates [23]. This film enables the use of triple-channel dosimetry, where the

optical density is measured in the red, green, and blue visual channels, which allows for more accurate dosimetry than a single-channel method, which only measures optical density using one channel [23], [24].

Once the film has been exposed it is self-developing, so no post exposure treatment is required [22], [23]. This self-development takes time and causes changes in the film, so in order to get accurate readings from the film the time between exposure and scanning should be at least four times the time that elapsed between the exposure of the first pieces of film and the last [25]. Time between film exposure and film scanning varies from 24 to 72 hours [24], [26], [27].

The GAFChromic protocols for film calibration and dosimetry have been published by Ashland in order to ensure accurate and reproducible use of their film [25]. The film has some polarization qualities so the film must be scanned in the same relative orientation. A marker may be used to indicate the direction on the film if it is being cut to ensure the orientation is consistent when the films are scanned (Figure 12) [23], [24]. The scanner may also have different responses along the bed of the scanner so film should be scanned along the same portion of the bed, and the scanner should be sufficiently warmed up to ensure consistent scans [24], [25]. The scanner should be set to the following parameters: professional mode, film transparency, positive film, 48-bit colour, and a resolution of 50 or 72 (although higher resolutions are also capable but are not typically necessary for dosimetric purposes) [25].



Figure 12: Photo of two pieces of film, with the direction marked with an arrow (for scanning direction) and the name of the measurement

The software FilmQAPro is recommended for dosimetry and has features included to create calibration curves and analyse film [25]. To create a calibration curve, several pieces of film must be exposed at different dose values including one at 0 Gy. The calibration curve should extend to higher doses than those you intend to measure but is valid for the entire range [25]. The calibration curves are best fit with a dose range that follows a geometric progression, and the calibration curve is only valid for film from the same lot [25]. Once the designated time elapses from when the film is exposed, irradiated samples should be scanned and imported to FilmQAPro (this elapsed time should be consistent for all following measurements taken) [25]. Once imported into FilmQAPro, the included calibration curve tool can be used to create the calibration curve which is then used for future dose measurements using the film.

Due to the dye in the active layer, there is no clear portion of the film which gives it an advantage in the effective dose range of the film [23]. The

program is able to read the saturation levels for the three colour channels (red, green, and blue) [25]. Using the input of the known dose to the film, the program is able to assign colour saturation data to dose values and create calibration curves for each colour channel using a function with the form:

$$d_x(D) = a + \frac{b}{D - c}$$

Where $d_x(D)$ is the optical density of the film for each channel x at dose D with parameters to be fit (a , b , and c) [23].

1.5. 3D printing

1.5.1. Types of 3D printing

The first 3D printing technology was invented in the 1980s and is called stereolithography (SLA) and uses UV photons from a laser to cure the surface of a photo-curable liquid monomer bath [28]. The 2D cross sections of an object are traced using the laser to create a solid 2D layer of the desired 3D object [28]. Selective laser sintering (SLS) was developed during the emergence of SLA and used a laser to sinter areas of powdered material to create an object [28]. Inkjet printing was being developed at the same time and used a technique of layering powdered material and a binder to create objects, but this technique often required post processing to ensure structural integrity [28]. Fused deposition modeling (FDM) is the printing method which uses thermoplastic filament which is heated and then extruded in layers to create objects [28].

A more recent technique is Metal Jet printing, which uses a method like inkjet printing but with powdered metals [29]. The metal powder is layered on the base plate and then a printing agent is used to bind the powder together in the shape designed for that layer of the object [29]. Once all layers have been printed the object has the excess metal powder removed from the surface and is then sintered to create a solid piece of metal [29]. Once the finished object is cool, any post processing finishing (e.g. smoothing, polishing) can be performed and the object is complete (Figure 13) [29].

All 3D printers use files generated by computer-aided design (CAD) software [28]. The CAD file defines the geometry of the layers and communicates with the printer to provide the specifications for the printing speed, temperature, and design among other necessary specifications for the 3D printer and technique being used [28].

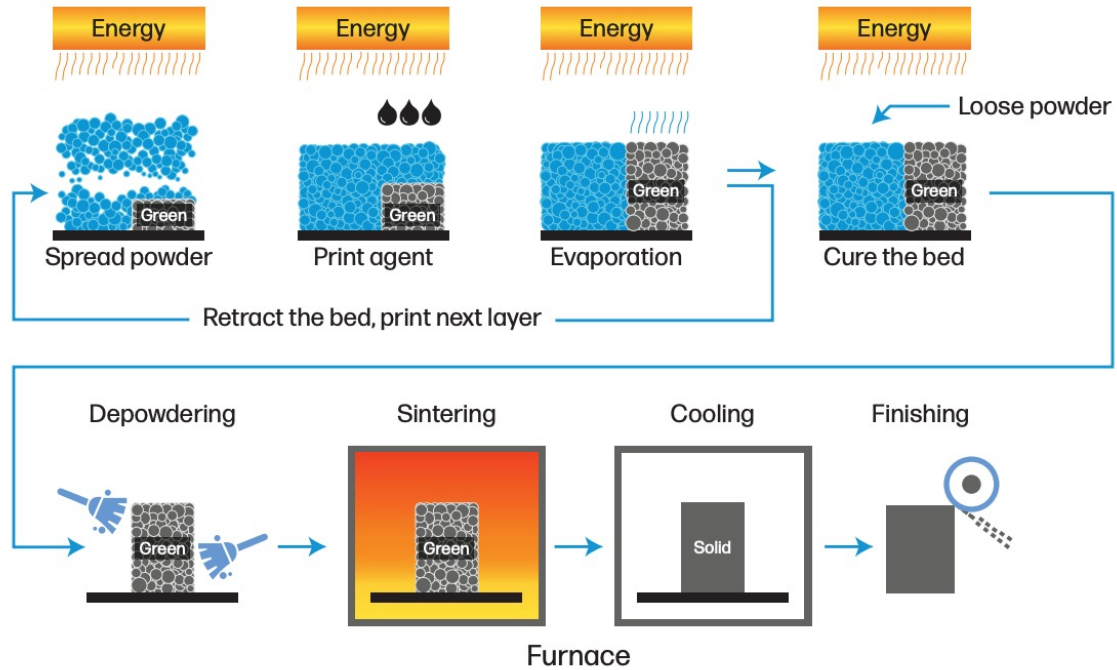


Figure 13: HP Metal Jet printing process[29]

1.5.2. 3D printing in gynecological brachytherapy

The use of 3D printing in gynecological brachytherapy is relatively new, and can be used to improve dose distribution and experience of the patients [26], [30]–[33]. Non-standard geometries of applicators have been made to improve the fit to patients [26], while others are using 3D printing to modulate dose delivery [30], [34]. Printing patient-specific sizes and geometries of applicators allows for a more comfortable and accurate fit, particularly if the patient is between commercially available sizes. If the applicator is too small, it may slip or move between imaging and treatment, and if the applicator is too large, it could cause discomfort and other dose distribution difficulties [26]. Printing a multichannel applicator also allows for customized channels along a patient specific shape [35].

Using a water equivalent 3D printing material, ensures that the planning software does not need to be modified if it uses TG-43 formalism for dose calculation. All the dose calculations can continue as they did previously, as commercially available applicators are also made of water equivalent materials. 3D printing allows for sizes to be specified to each patient, and if using interstitial guides these can also be specified to patient anatomy and geometry to allow for more optimal catheter placement [26], [31]. Sethi *et al.* created three 3D printed applicators based on three patients' anatomical needs (Figure 14). A single channel vault was created with a diameter between available sizes (2.75 cm) for an optimal fit, a small diameter (2 cm) applicator was created with a central catheter channel as well as external grooves for guiding interstitial catheters, and a large applicator (3.5 cm) was printed with a central channel for a tandem as well as external grooves for surface catheters [31]. The ability to safely and accurately, plan and treat patients with 3D printed applicators allows for a larger range of patients to be treated to the same standard [26], [31].

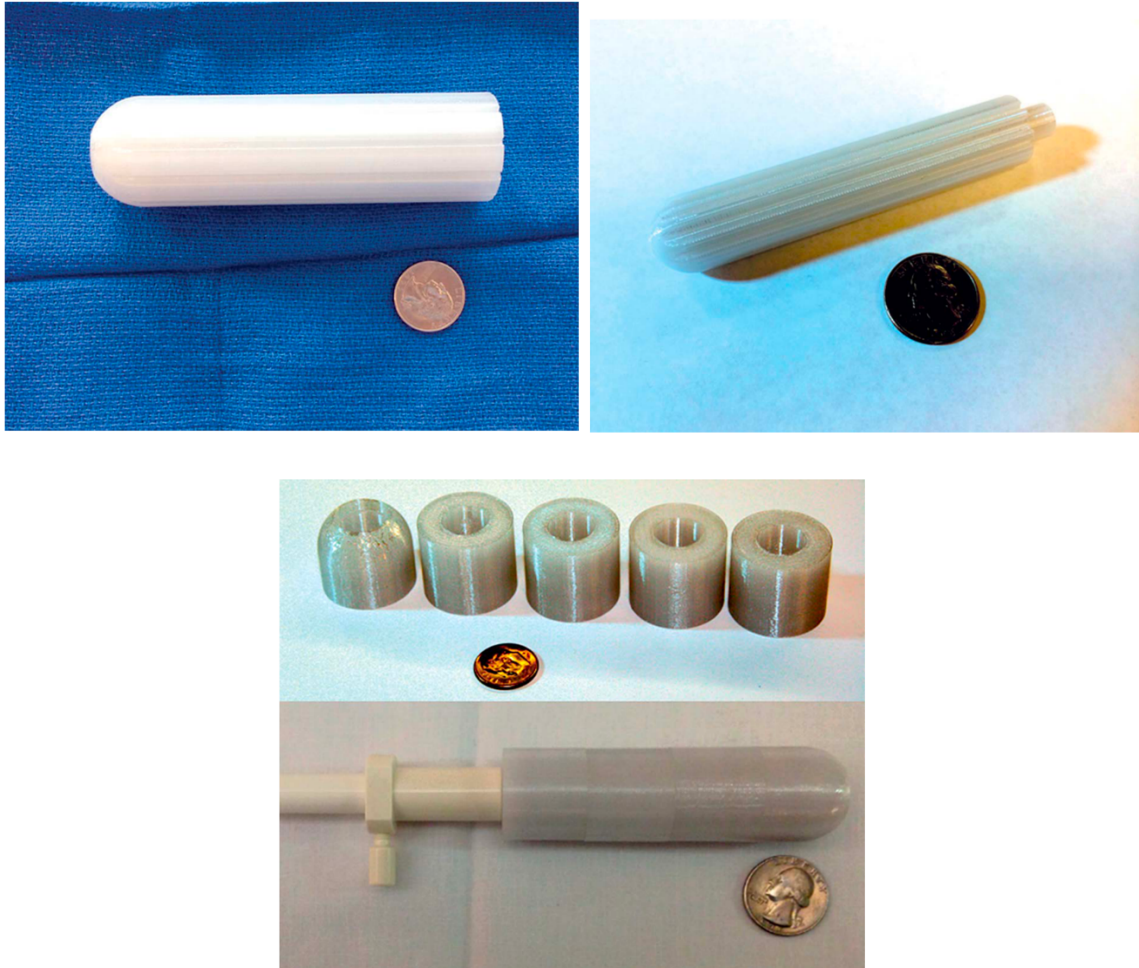


Figure 14: Custom 3D printed applicators from Sethi et al. Top Left: 3.5 cm diameter applicator with 10 external catheter channels and a central channel, Top Right: 2 cm diameter applicator with 6 external catheter channels and a central catheter channel, Bottom: 2.7 cm diameter segmented cylinder with a central channel

3D printed applicators can also be used to replace generic interstitial templates. Interstitial applicators and external templates can be printed for personalized dose distributions [35]–[38]. Custom interstitial needles guides printed on the ring of a ring and tandem style applicator, this style could also be adapted for patients with a narrow vagina and another solution was to use a

cylinder with custom channels [38]. These printed applicators improved the treatment delivered to the tumours, without exceeding the dose delivered to nearby organs [38]. Garg *et al.* created an algorithm to generate custom implants for custom catheter guiding and source positioning (Figure 15). The implants would have a geometry such that air gaps would be minimized and it would fit securely inside [35]. The custom channels created by the algorithm allow for better coverage due to the increase in possible dwell positions near the tumours resulting in less tissue outside the target area being irradiated [35]. Sekii *et al.* designed interstitial vaginal applicators that could also have a perineal interstitial template. These printed applicators were able increase the ease of treatment and reduce pain during treatment [37].

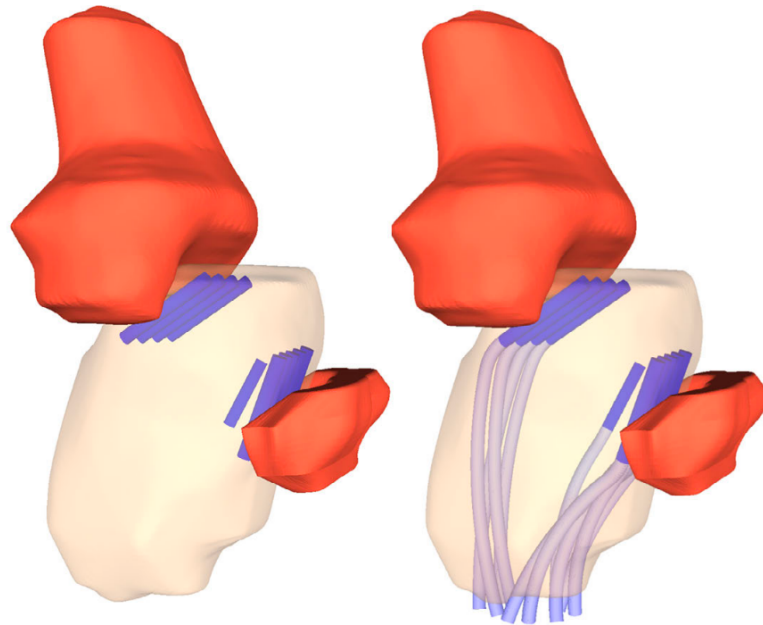


Figure 15: 3D printed implant (transparent orange shape) with dwell segments (left) and the computed channels using their algorithm (right) from Garg et al.

3D printing techniques can also be used to incorporate shielding into applicators, creating altered dose distributions. Using shielding that is consistent along the length of the applicator allows for the shielding portion of the applicator to be removable, enabling imaging done with the outer portion positioned in the patient (Figure 16) [34]. Figure 17 demonstrates an asymmetrical shielding geometry that is maintained along the length of the applicator. The dwell time at C is extended to increase the size of the isodose lines to treat more area, whereas at B the dwell time is decreased or eliminated to shrink the isodose to avoid irradiating nearby organs [33]. Many shielding geometries allow for this removable section and can provide shielding to desired areas, as well as modify the dose distribution along the length of the applicator by increasing dwell times at desired locations [34]. This type of orientation allows for decreased dose in chosen areas, but ultimately the dose to non-target volume tissue will still occur. A different shielding orientation would be to print an applicator that shields in all directions except for the target volume (Figure 18) [30]. The applicator in this instance would remain as one solid piece, but the shielding in areas you do not wish to treat can be greatly reduced [30]. The material used for the shielding is only limited by the printing capabilities available and high-density materials able to be printed [30], [33].

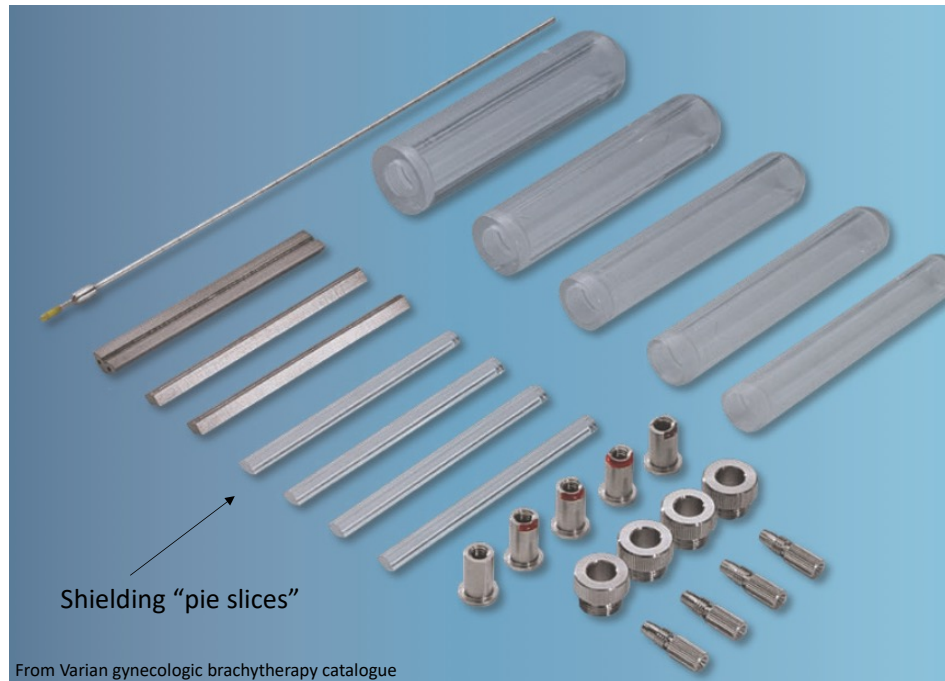


Figure 16: Varian applicators and shielding from the Varian gynecologic brachytherapy catalogue [39]

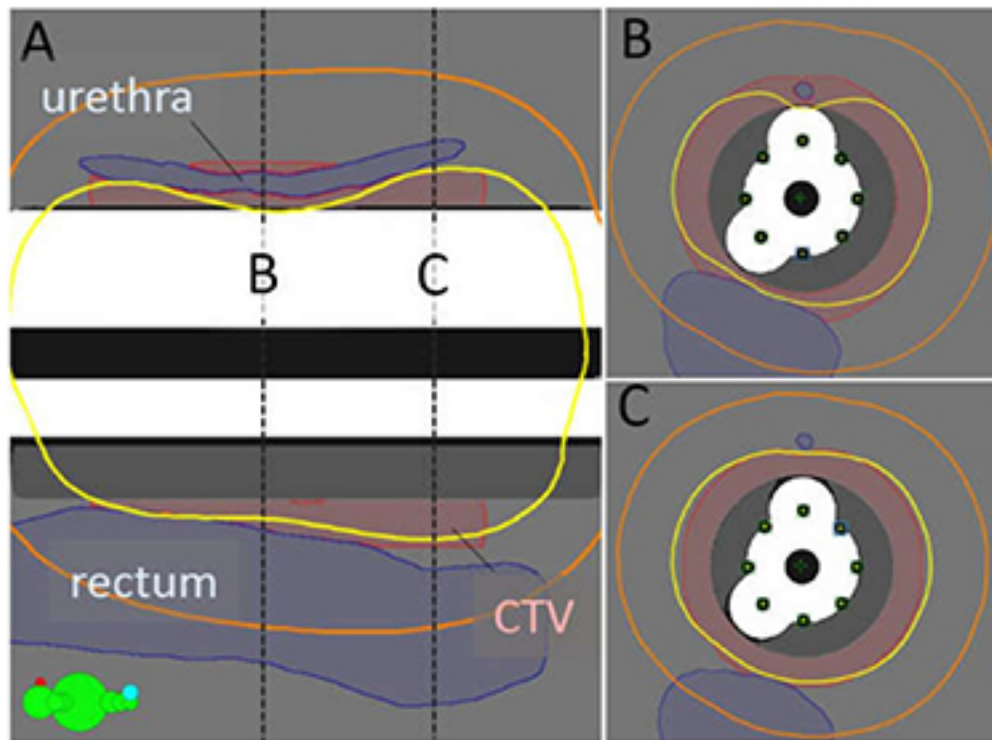


Figure 17: Demonstration of isodose manipulation using shielding and dwell time [33]

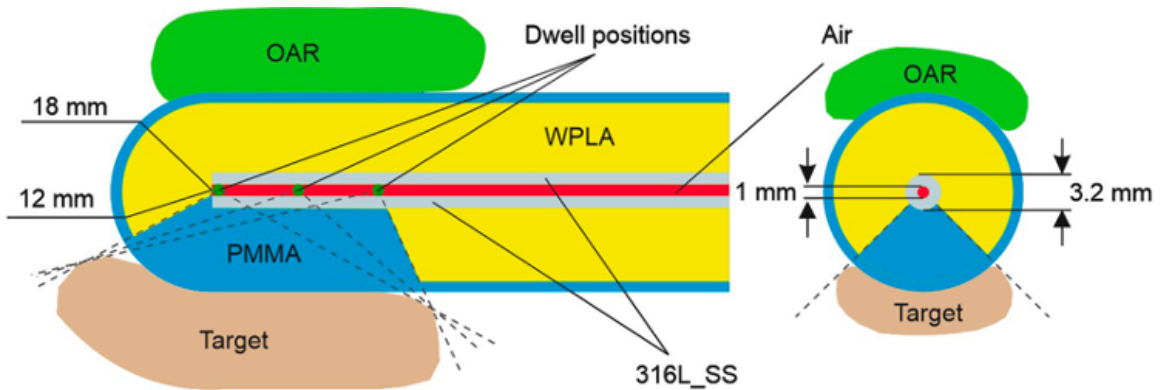


Figure 18: Theoretical shielded applicator design, shielding in all directions that do not contain the target [30]

These two methods have two different workflow connotations. Shielding material, because it is dense, causes shadows and streaking to occur when imaged. With a two-part applicator, imaging can be performed as with a water equivalent applicator. The shielded core can then be switched into the applicator, while maintaining applicator and patient position. With an applicator where the shielding cannot be removed, imaging cannot be done as you would with the shielded applicator in place. This would require more steps in the workflow to account for the placement of the applicator but would generally provide more shielding than the first applicator. An applicator that uses a shielding geometry core that can be removed has the same shielding geometry along the length of the applicator. This means the shielding core geometry is limited by the location of the treatment volume, as you wouldn't want to shield in the direction you wish to treat. An applicator that does not allow for the shielding part of the applicator to be removed allows for shielding geometry to be different along the length of the

applicator, providing extra shielding to areas that may not have it if the removable applicator were to be used.

1.5.3. Materials in 3D printing

When creating an applicator for intracavitary brachytherapy, the applicator must be biocompatible and sterilizable. Some common methods for sterilizing applicators include steam (using an autoclave), ethylene oxide (EtO), and hydrogen peroxide (H₂O₂) [34]. One major issue with steam sterilization is the temperature, as 3D printed materials are created by heating the material in order to print objects. The materials have different sensitivities to temperatures, and some are more susceptible to the high temperatures needed for steam sterilization (PC-ISO [40], ABS-M30i [41], and MED610 [42] for example). Depending on the sterilization method used, some materials may be excluded from consideration. The sterilization may also have an effect on workflow, as steam sterilization is faster than both EtO and H₂O₂ sterilization methods [43]–[45].

The effect these materials have on dose is not equal. Many plastics show water equivalency in the relevant energy region [26], [30], [46]. There has also been some work using tungsten powder mixed with a 3D printing plastic powder in order to print a high-density object capable of dose shielding [30], [34]. The ability to use water equivalent printing material as well as shielding material would allow the user to print an applicator with sections capable of typical treatment doses and shielding capabilities. There are also some new technologies

that allow for metals themselves to be printed without the need for the powder to be mixed with plastic [29].

Semeniuk *et al.* analysed the shielding capabilities of many 3D printing materials using Monte Carlo simulations. All the materials investigated are biocompatible and suitable for use in brachytherapy applicators [30]. They had a range of densities and mass attenuation coefficients, but the printing plastics were all similar in both areas (1-1.32 g/cm³, and ~0.1 mass attenuation coefficient) [30]. The stainless steels also showed similarities to each other and the most dense material investigated was a mixture of the printing plastic PLA and powdered tungsten (WPLA) [30]. Figure 19 shows the dose profiles in water using all the different materials in a generic applicator (Figure 20), the plastics were similar to the dose distribution in water, but the steels and WPLA provided 11% and 56% shielding, respectively, at 5 mm from the applicator surface [30].

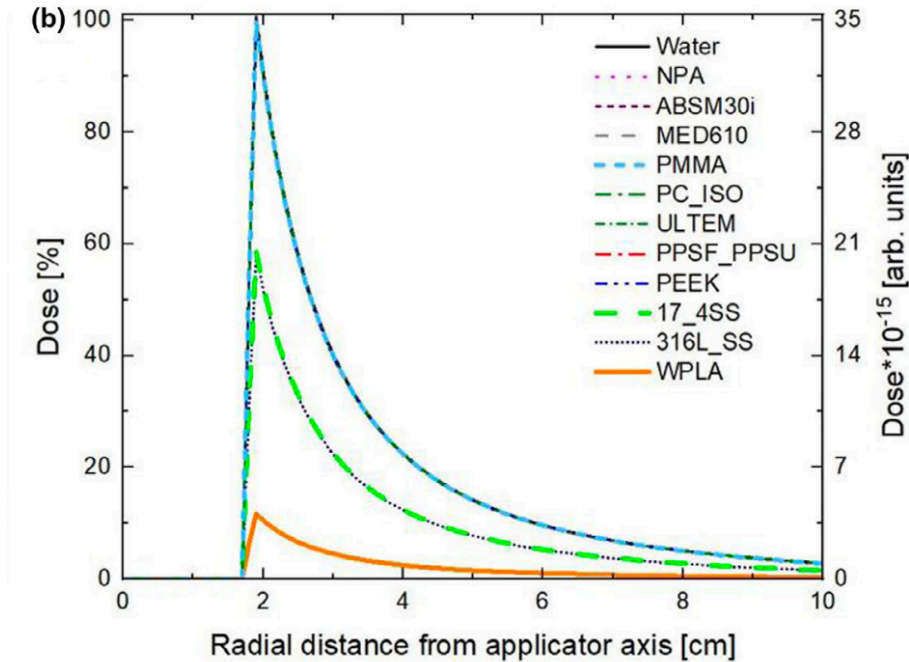


Figure 19: The dose profiles of water and all investigated 3D printing materials

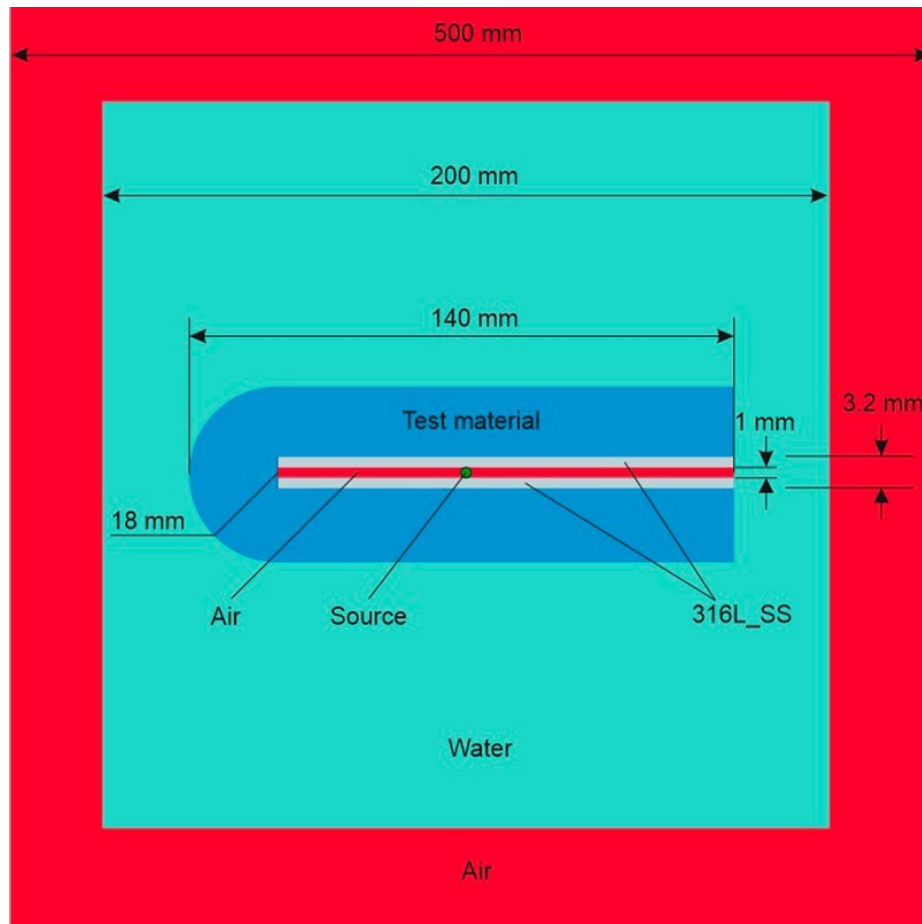


Figure 20: Generic applicator based on TG-186 [30]

Pera *et al.* uses film and an ionisation chamber for validation of 3D printed materials and their attenuation compared to water using an Ir-192 source from Varian. Frames for holding film were printed in the desired material, which was then submerged in water and irradiated exposing the film and collecting a depth dose profile which was compared to that of water [47]. A custom phantom was also created to validate materials using an ionization chamber [47]. The phantom is several boxes used to hold the material to be validated, the source, and the ionization chamber [47]. The depth can be varied, and a depth dose curve can be created with the data from the ionization chamber [47]. The depth dose attenuation can then be compared with that of water [47]. These methods both

found that the materials tested were very similar to water (within 3%) and that the largest influence on dose variation was the distance from the source rather than the material in this phantom set up [47].

1.6. Monte Carlo Simulations

1.6.1. Egs_brachy

The code used to run the Monte Carlo simulations described in this work is the EGSnrc Code System (Electron-Gamma-Shower from the National Research Council Canada) [48]. The base system is capable of realistically simulating radiation transport of electrons and photons through any material and is the gold standard for dose calculations [48]. The program uses source distribution descriptions as well as probability distributions from the total interaction cross section in order to determine particle travel distance to interactions [48]. The differential cross section determines what interaction occurs when there is an interaction [48]. This process is repeated until all particles are absorbed, or they leave the geometry of note [48]. EGSnrc is based on the EGS4 system but has had many changes made, including the use of the condensed history method[48]. This method combines transport and collision processes into a single “step”, understanding that most individual interactions do not cause large changes to the particle’s energy and direction of movement [48]. A set of energy, direction, and position changes are sampled at the end of a step, so the simulation is dependent on this step parameter in order to run [48].

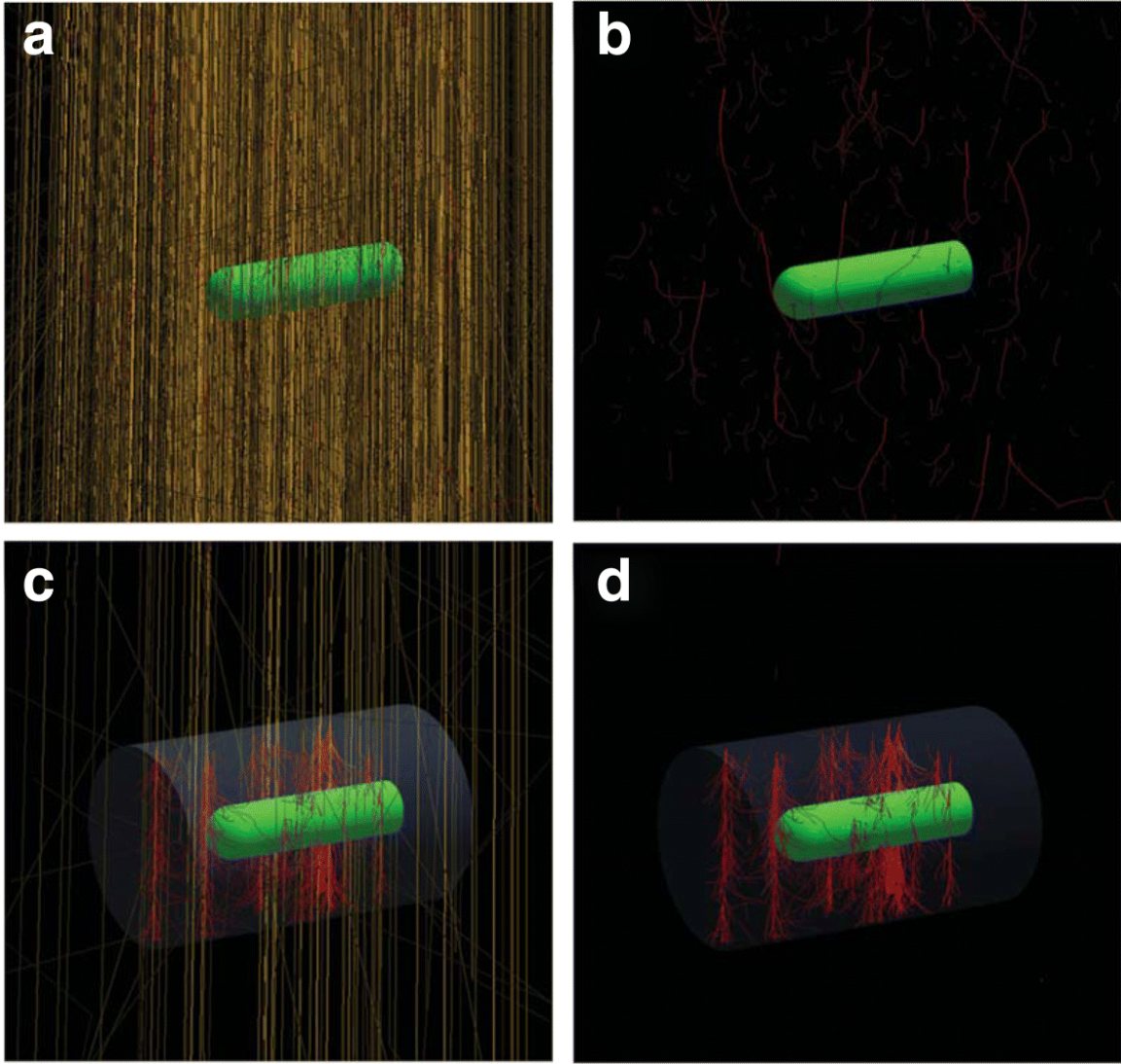


Figure 21: Particle tracking using Monte Carlo EGSnrc package `egs_chamber` a) normal particle transport of an ionization chamber, b) secondary electron tracks in (a), c) transport using cross-section enhancement in a volume around the chamber, d) secondary electron tracks in (c) [49]

The brachytherapy package within EGSnrc is called `egs_brachy`. In order to combat the loss of accuracy, due to tissue inhomogeneity, when using TG-43 dose calculations, many have adopted model-based dose calculation algorithms [50]. Two examples of commercially available treatment planning algorithms are

the Acuros in Brachy Vision and ACE in Oncentra Brachy [50]. These two algorithms differ in their methods, Acuros is a grid-based Boltzmann equation solver, and ACE is a collapsed cone superposition/convolution method [50]. Monte Carlo is recognized as highly accurate but lacks accessible and user-friendly code, and often requires long computational times [50]. User code existed, beginning to bridge the gap, and this along with the release of the egs++ library (EGSnrc C++ class library) motivated the development of egs_brachy [50]. Egs_brachy can benefit from all EGSnrc code (dose calculations, geometry models, efficiency enhancements, variance reduction techniques etc.) and it has brachytherapy specific dose calculations, source definitions and spectra, and applicators [50]. Figure 22 shows that EGSnrc calculations account for material heterogeneity when TG-43 formalism (treatment planning system, TPS) does not. The dose profiles agree in the water phantom but in the CT phantom where there is tissue heterogeneity, the Monte Carlo simulation is able to account for the differences and produce a more accurate dose profile.

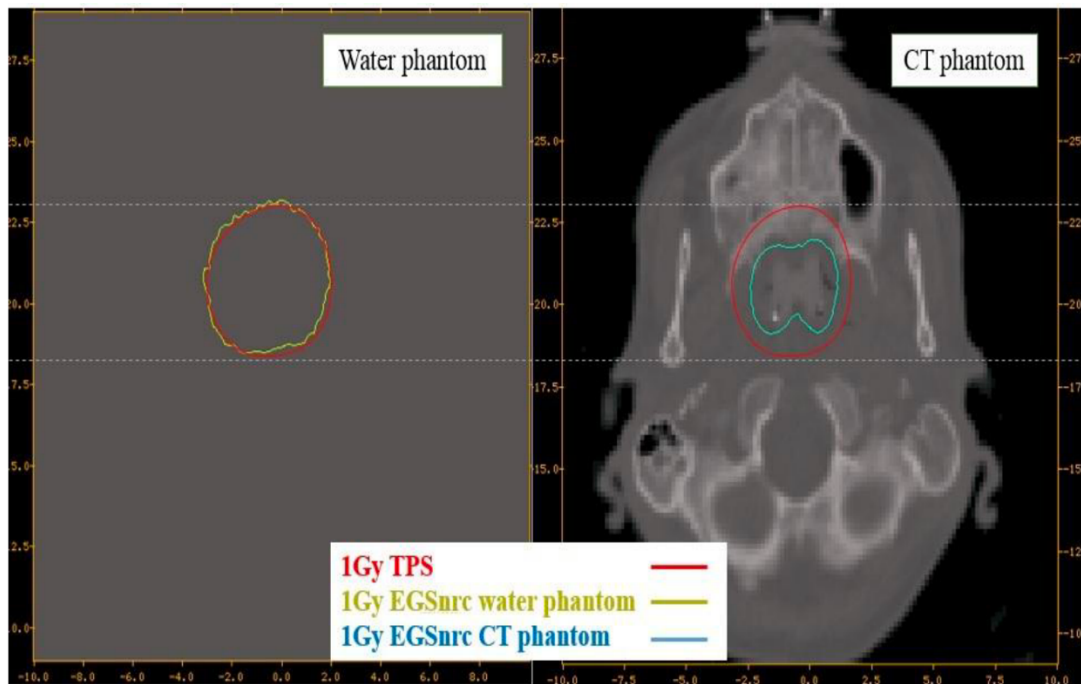
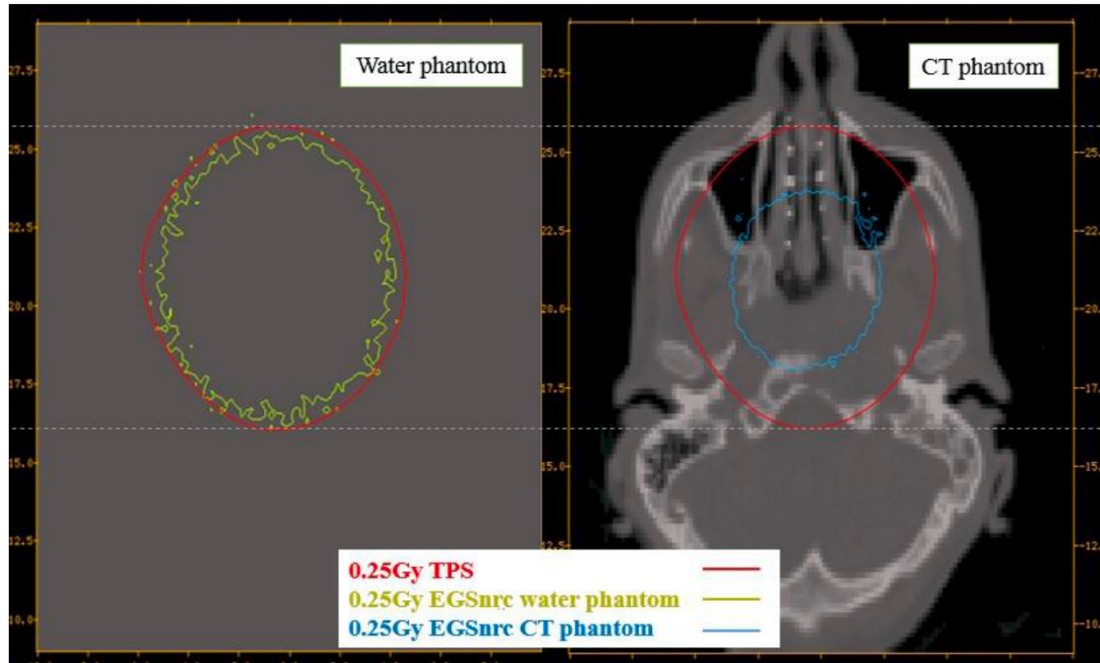


Figure 22: Two examples of Monte Carlo simulation (EGSnrc) and treatment planning system (TPS, using TG-43 formalism) dose profiles being compared in water phantoms and in CT phantoms

2. Methods and Materials

This work aimed to characterize the shielding capability of 3D printed metal samples. Quantifying how the dose decreases with the thickness of the metal would allow for future use of the 3D printed metals in personalized applicators. Using film and simulations, the shielding capability will be measured and compared through multiple methods.

2.1. Metal Samples

Metal samples were provided by Hewlett Packard, HP, Palo Alto, California, in thicknesses ranging from 1-5 mm. They were all 3D printed with the same stainless steel. They were initially printed to a nominal thickness and then ground down to the various desired thicknesses. Independently-verified measurements of the sample are shown in Table 2

Table 2: Measurements for all provided stainless steel samples from HP.

Size	Weight [g]	Length [mm]	Width [mm]	Thickness [mm]	Density [g/cm ³]
1 mm	21	54.36	54.03	1.07	6.68
1 mm spare	25	54.54	54.40	1.18*	7.14
2 mm	47	54.48	54.25	2.02	7.87
3 mm	69	54.12	54.35	3.01*	7.79
4 mm	147	54.50	54.5	6.37	7.77
5 mm	146	54.53	54.49	6.30	7.80

As shown above, samples marked as 4 mm and 5 mm were mistakenly not ground to the appropriate dimensions. These two samples were then removed from further investigation. In order to perform measurements from 1 mm to 5 mm, the other samples were used in combination to achieve the desired thicknesses. The thickness measurements with asterisks (*) showed evidence of inconsistent thickness across the sample. The thickness measurements stated are as measured with calipers at the edge of the sample. The average length and width of the samples are 54.46 mm and 54.32 mm respectfully.

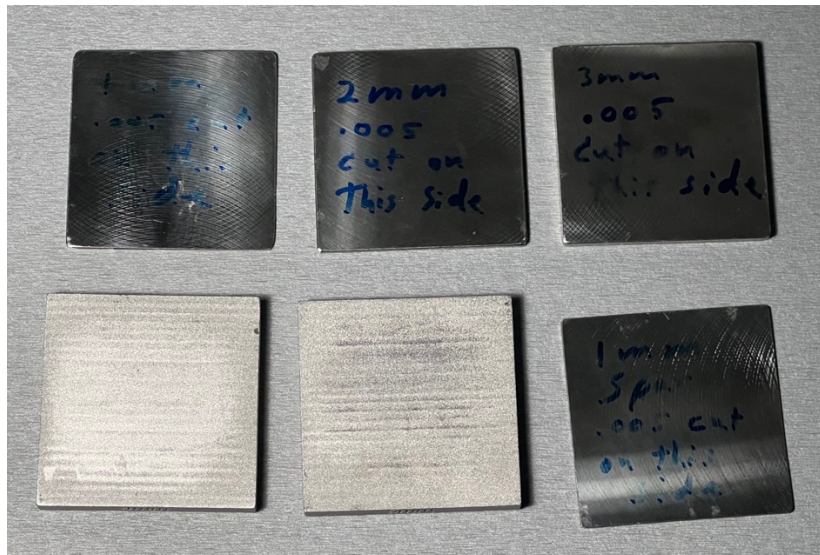


Figure 23: The metal samples (from left to right, top to bottom: 1 mm, 2 mm, 3 mm, 4 mm, 5 mm, 1 mm spare)

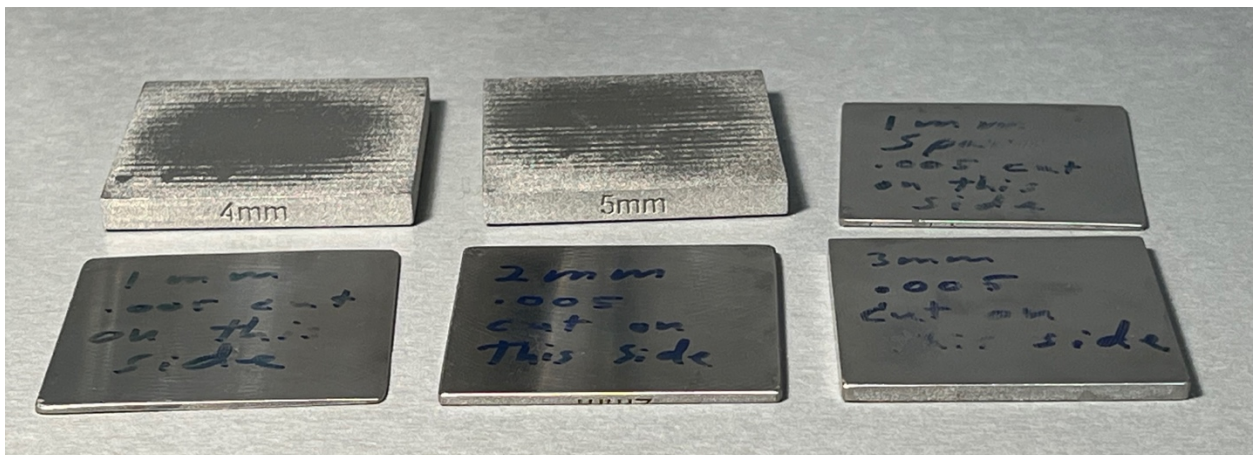


Figure 24: Metal sample thicknesses (from left to right, top to bottom: 4 mm, 5 mm, 1 mm spare, 1 mm, 2 mm, 3 mm)

2.2. Custom Solid Water Phantom

A solid water phantom with dimensions 30 cm x 30 cm x 1 cm was modified in order to insert the metal samples. An indentation was cut into the phantom with the dimensions of the samples (5.5 cm x 5.5 cm) and a thickness of 5 mm. The material

that was removed was cut into 1 mm slices in order to eliminate air space when metal samples of thickness less than 5 mm were used. This phantom was used in all film measurements when the metal was being used.

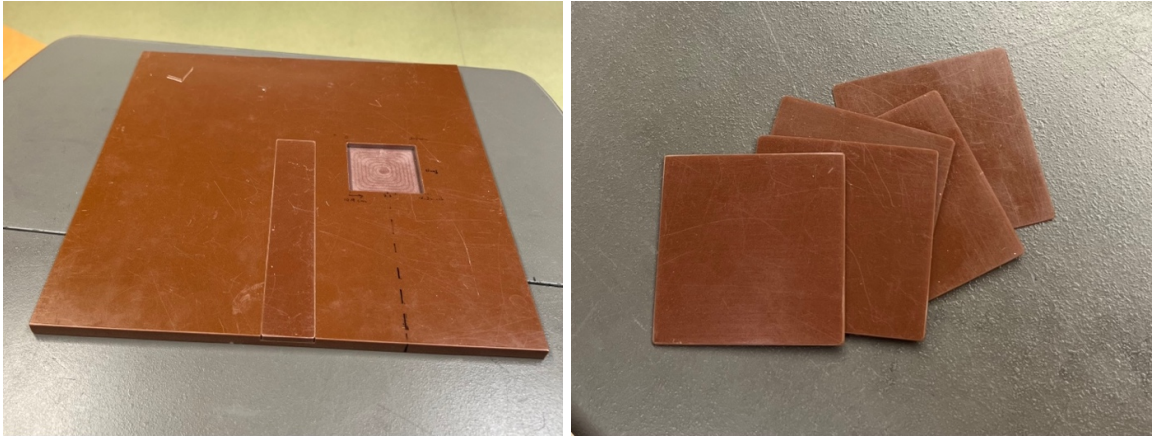


Figure 25: The custom water phantom with the hole for the metal samples and the five 1 mm pieces of solid water used to fill the air gaps.

2.3. Film Set Up

The film used for all measurements was EBT3 film (Lot 03082201) from Ashland (Wilmington, Delaware). The source used is a MICROSELECTRON V2 Ir-192 source (Alpha-Omega Services, Inc., Edgerly, LA) housed in an HDR remote afterloader (Nucletron, Elekta, Stockholm, Sweden).

2.3.1. Calibration Measurements

To position the catheters in the solid water phantom, a 30 cm x 30 cm x 1 cm solid water phantom with catheter cut outs was used. It has seven grooves for holding the closed ends of catheters inside the phantom (Figure 26). The central three were used for the measurements. The catheters were placed, and masking

tape was used to secure them, so they did not slip when adjusting the phantom arrangement between film exposures.

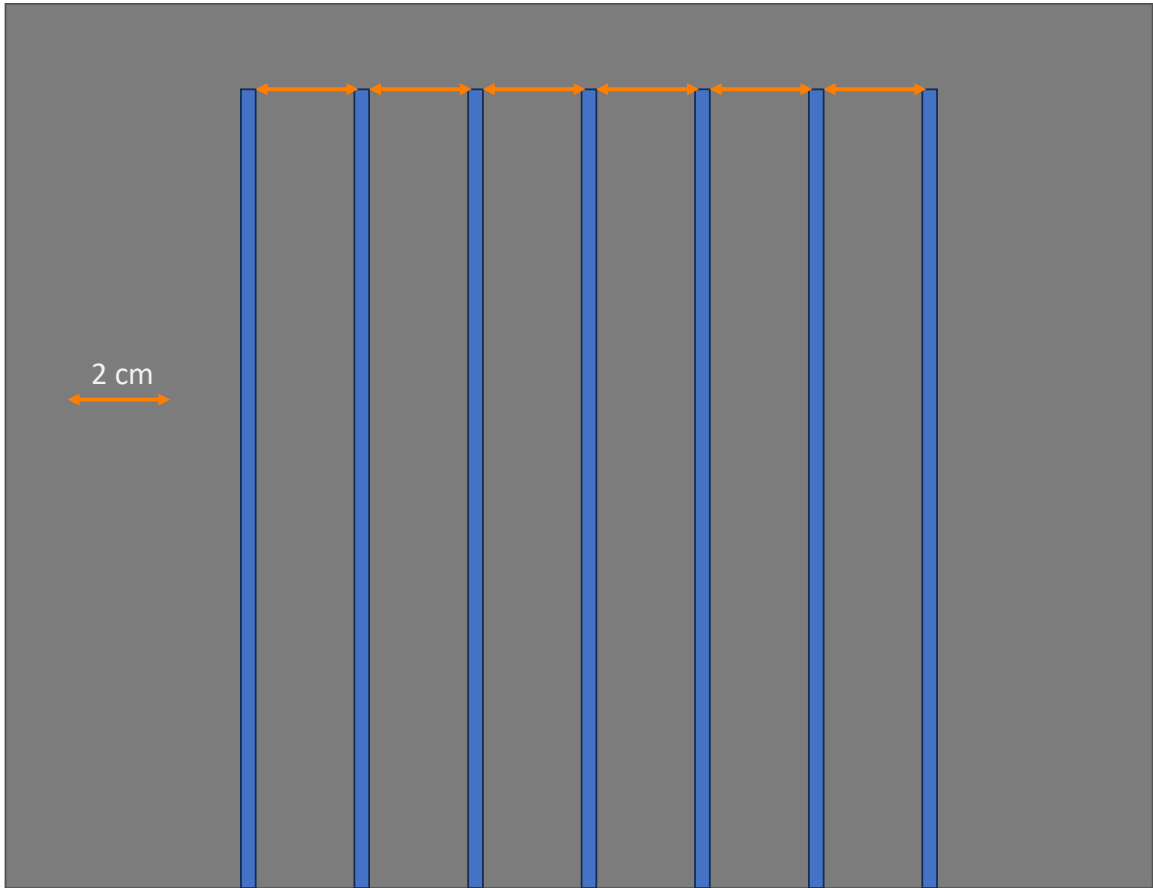


Figure 26: Diagram of the piece of solid water with the catheter cut outs (shown in blue) they were each 2 cm apart and tape was used to secure the catheters when they were placed

The film was placed 2 cm from the plane of the catheters for all planar measurements. This 2 cm separation consisted of additional solid water. Tape was used to mark the measured distances from the dose delivery plan on the phantoms to quickly reference the distances to shorten set up time. Some test measurements were taken to ensure proper placement of the film. The film was placed above the dwell positions as well in order to capture the maximum dose reading. Above the

film and below the phantom with the catheters, a 5 cm thick phantom was placed to provide adequate scatter conditions. (Figure 27)

The calibration dose values were scaled from the same plan used for the planar measurements, so they had the same seed orientation and relative dwell weights calculated using Oncentra Brachy (see Figure 31 and Figure 32). The calibration curve required scans to be taken at even dose intervals with a 0 Gy unexposed piece of film. Along with the 0 cGy piece of film, there were measurements taken at 100, 150, 200, 250, 300, 350, and 400 cGy. These films were then scanned three days after exposure, to allow for self-development and to accommodate scheduling requirements. They were then imported into the FilmQAPro software and a calibration curve was created using the included calibration curve creation program [25].

The film for all of the measurements were scanned on a different day than the calibration film, so calibration correction scans were needed. These were taken at 0 cGy and 400 cGy, (with only solid water present).

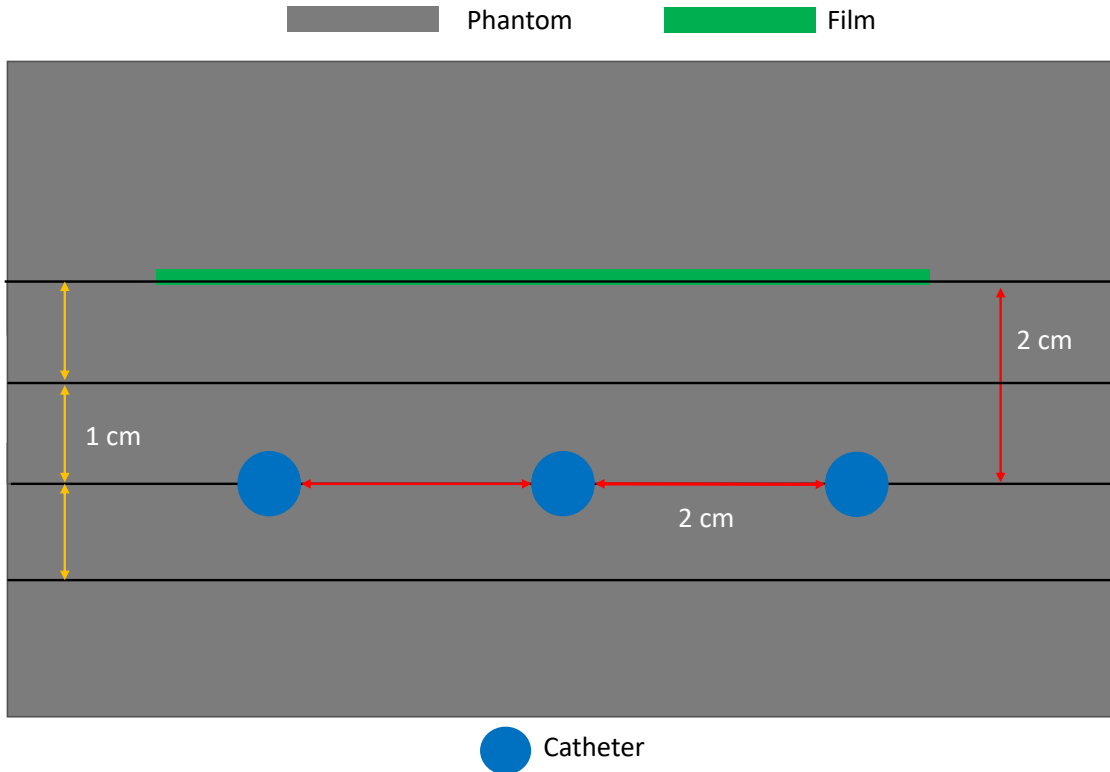


Figure 27: Graphic of the calibration set up

2.3.2. Planar Measurements

The planar measurements were taken using the same phantom orientation and film placement as the calibration set up. The measurements with the metal present were taken in two different arrangements. The custom phantom with the metal was initially placed so that the top of the metal was 1 cm from the catheters and 1 cm from the film (Figure 28). A second set of measurements were taken with the metal directly adjacent to the film, so the top of the metal was 2 cm from the catheters (Figure 29). When the metal pieces were inserted into the custom phantom cut-out, the extra 1 mm pieces of solid water were used to change the depth of the cut-out to match the metal sample (so using the 2 mm metal sample

the cut-out would have three 1 mm pieces of solid water followed by the metal placed on top).

The dwell positions for these measurements were all based on the same plan created in Oncentra Brachy (Elekta, Stockholm, Sweden). Using Oncentra Brachy, three catheters were placed with 2 cm of separation and dwell positions were specified every 0.5 cm along 4 cm of the catheter. The furthest dwell position was used so as to place the exposed area as near to the center of the phantom as possible. The time at each dwell position was calculated using the treatment planning software used at the QEII Cancer Centre, Oncentra Brachy (Elekta). The measurements with the metal samples were all taken with a dose value of 200 cGy delivered to 2 cm from the catheters, which was verified with a piece of test film which was exposed without any metal present.

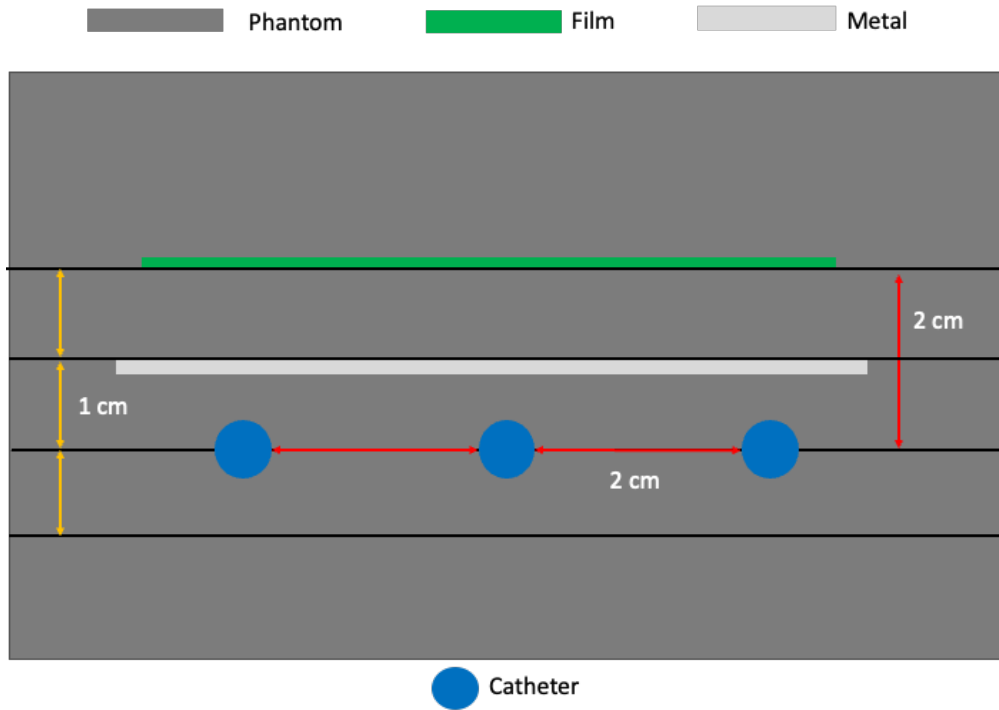


Figure 28: Graphic of the set up where the metal is halfway between the film and the catheters.

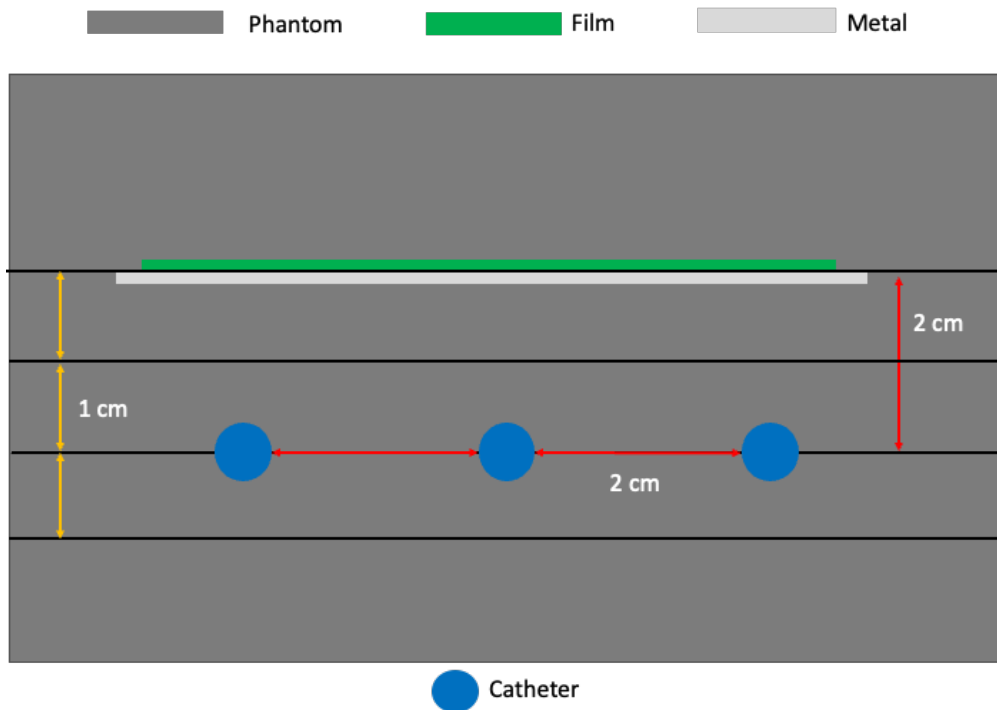


Figure 29: Graphic of the planar set up where the metal is directly adjacent to the film.



Figure 30: Photograph of assembled planar phantom, catheters are blue and inserted into the phantom via the grooves

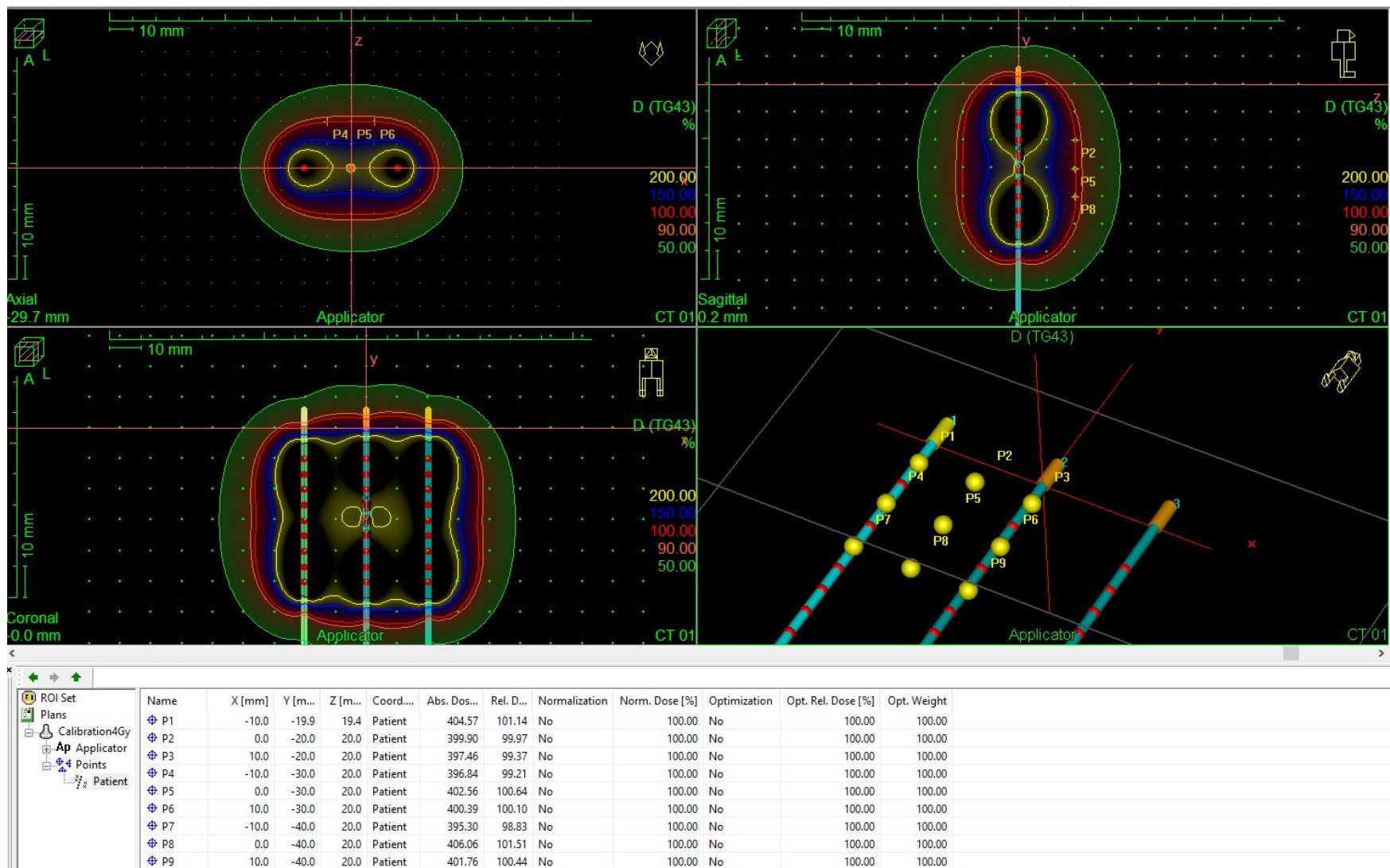


Figure 31: Oncentra view of the planar measurement treatment plan with the calculated dose values in a 2 cm x 2cm square that is 2 cm from the plane of the catheters. The dwell positions are highlighted with red dots along the blue catheters.

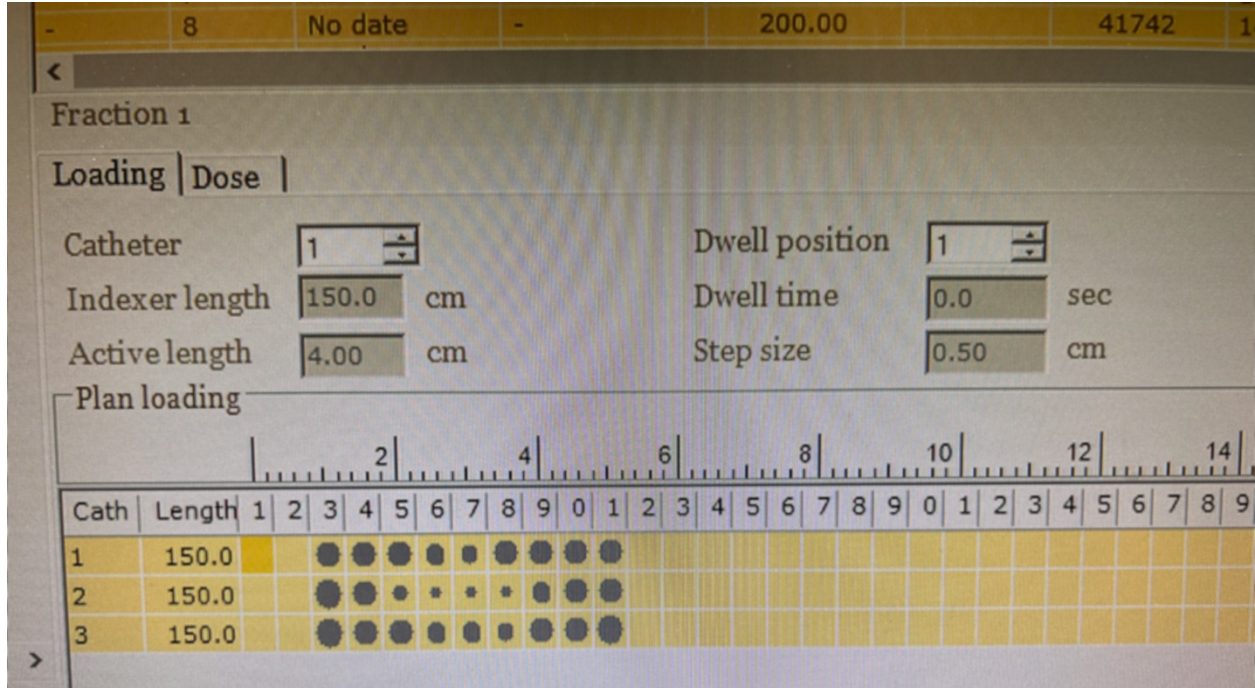


Figure 32: Treatment delivery system view of the catheters and their dwell positions as well as a visual representation of the dwell weights (larger circles have a longer dwell time than the smaller circles).

2.3.3. Depth Dose Measurements

The depth dose measurements were taken with the film perpendicular to the plane of the catheters, to get dose readings along the film at different distances from the source. The base of the set up matches the setup described earlier for planar measurements, with the 5 cm thick phantom underneath the phantom with the catheter cut outs. Above the phantom with the catheters, was the custom phantom with the metal samples. To capture 2 cm from the source, and to provide comparable results to the planar measurements, the film was positioned only 1 cm from the source to capture dose fall-off over the relevant region. The dwell position is listed in the Oncentra plan and this distance was used to

determine where to place the film. The edges of the film had some imperfections due to the preparation procedure so it was assumed the region closest to the source would contain inconsistencies in dose measurement. The film was taped to a 30 cm x 30 cm x 5 cm phantom, and it was stood on the 5 cm edge. Another of these phantoms was placed to sandwich the film between them and then the phantoms were taped together. Two more phantoms were placed on either side of the phantoms in order to achieve adequate scatter conditions. (See Figure 33)

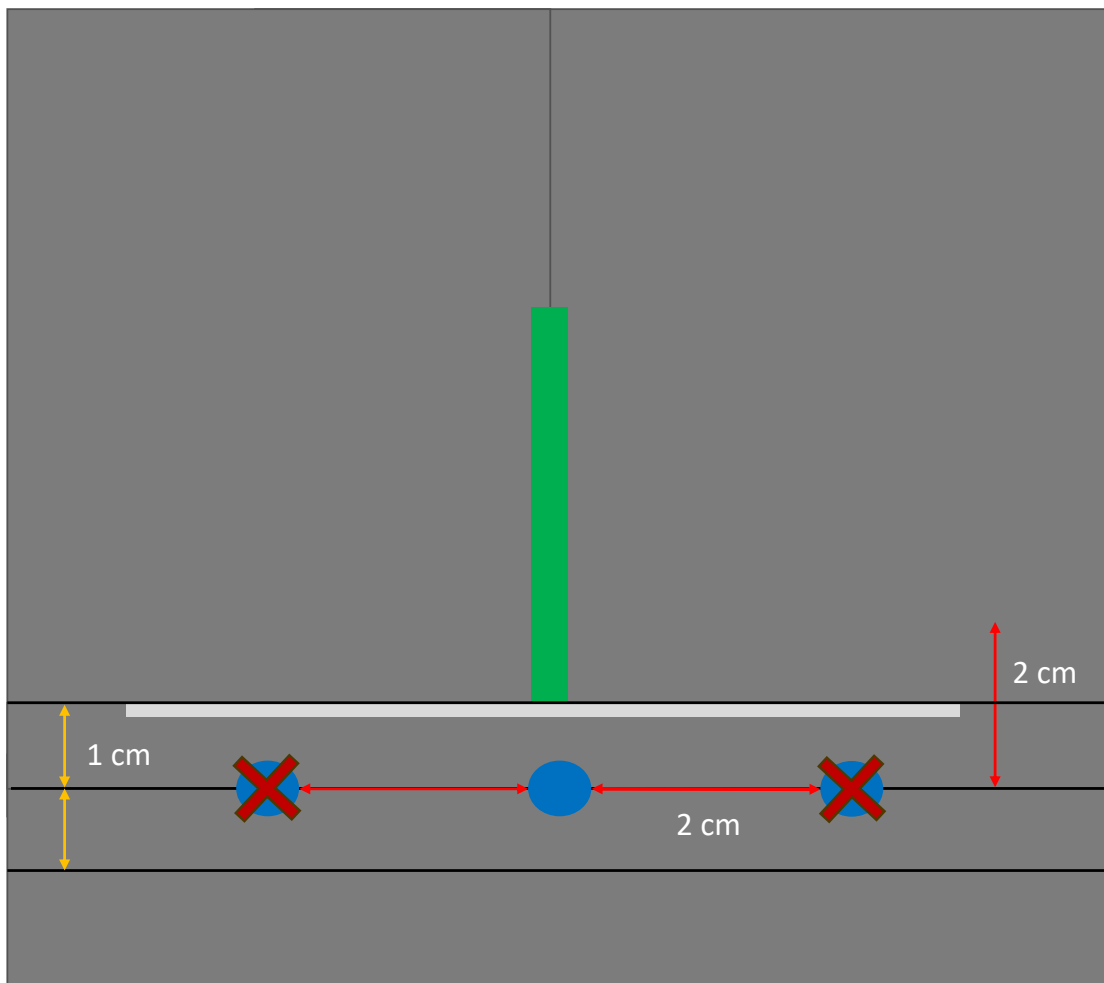


Figure 33: Graphic of the depth dose set up.

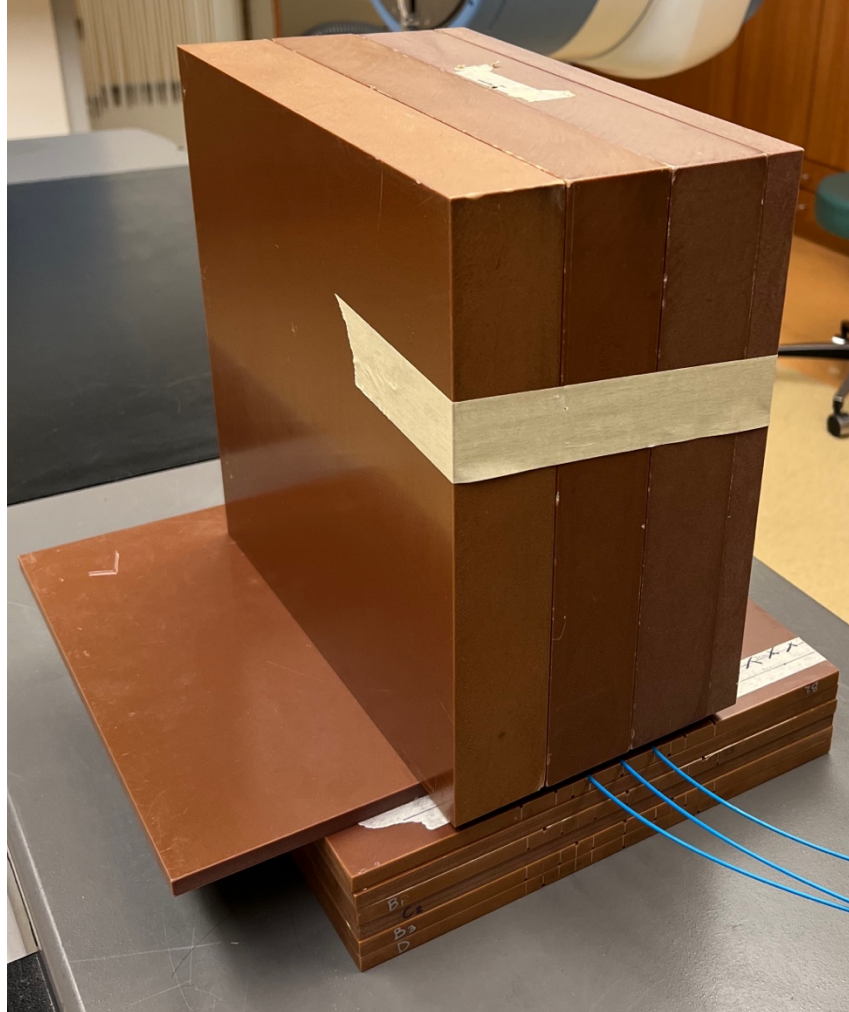


Figure 34: Photograph of the assembled depth dose phantom with blue catheters inserted into the base, and the film between the solid water that are stood up above the catheters

The depth dose measurements were taken using a single dwell position in the central catheter. The choice to do so was motivated by simplicity for modeling purposes, to provide a simple geometry to model with Monte Carlo and compare the results. The dose was set to be 200 cGy 1.5 cm from the source, as calculated in the Oncentra treatment planning system. The points measured in the planning software along the perpendicular direction are at 1 cm intervals. The dwell position was placed 3 cm from

the first dwell position of the catheter and this distance was used to determine the placement of the film.

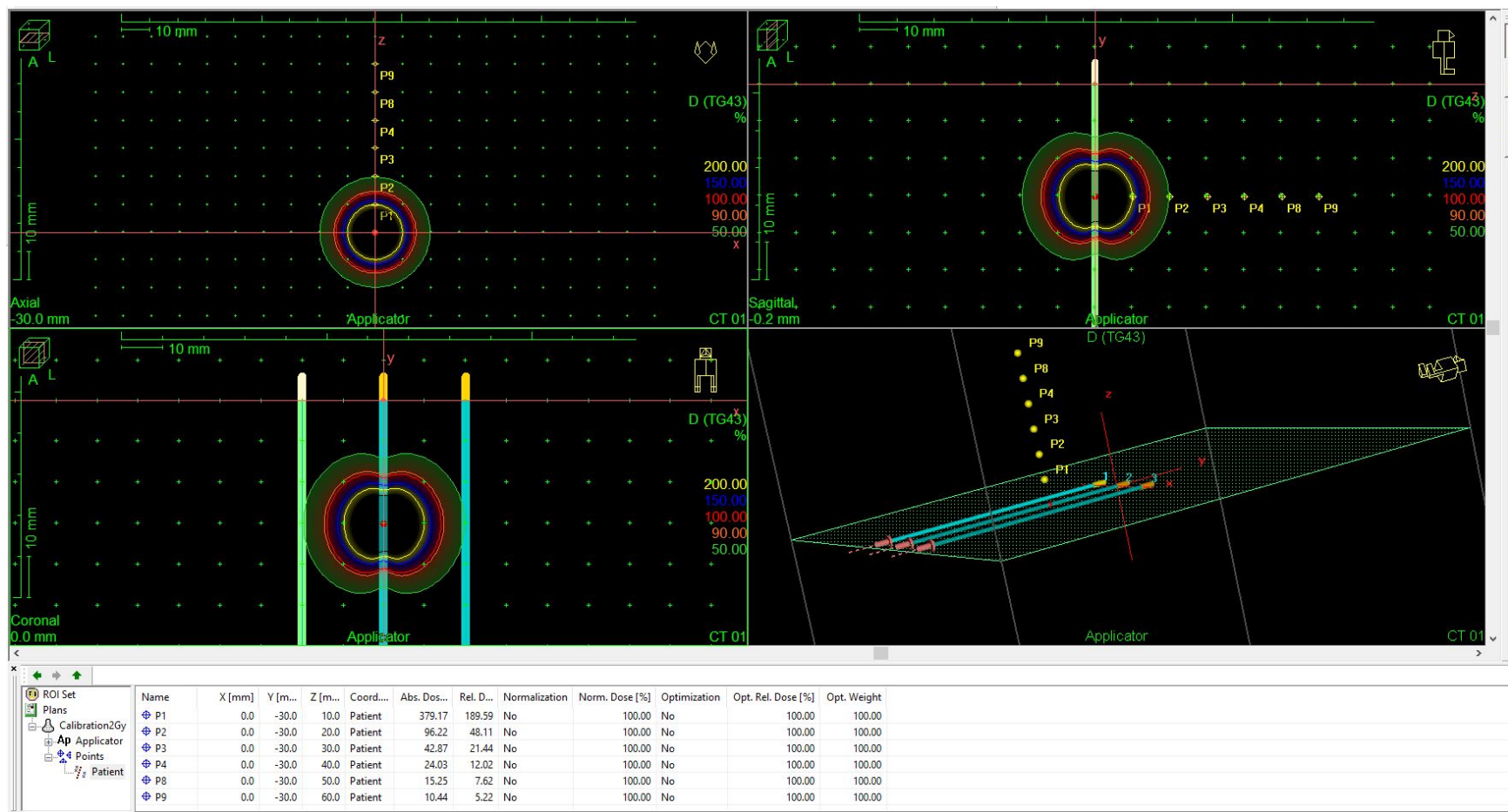


Figure 35: Oncentra view of the depth dose measurement treatment plan with the calculated dose values along a line perpendicular from the catheters. The dwell position is highlighted with a red dot in the central catheter (blue).

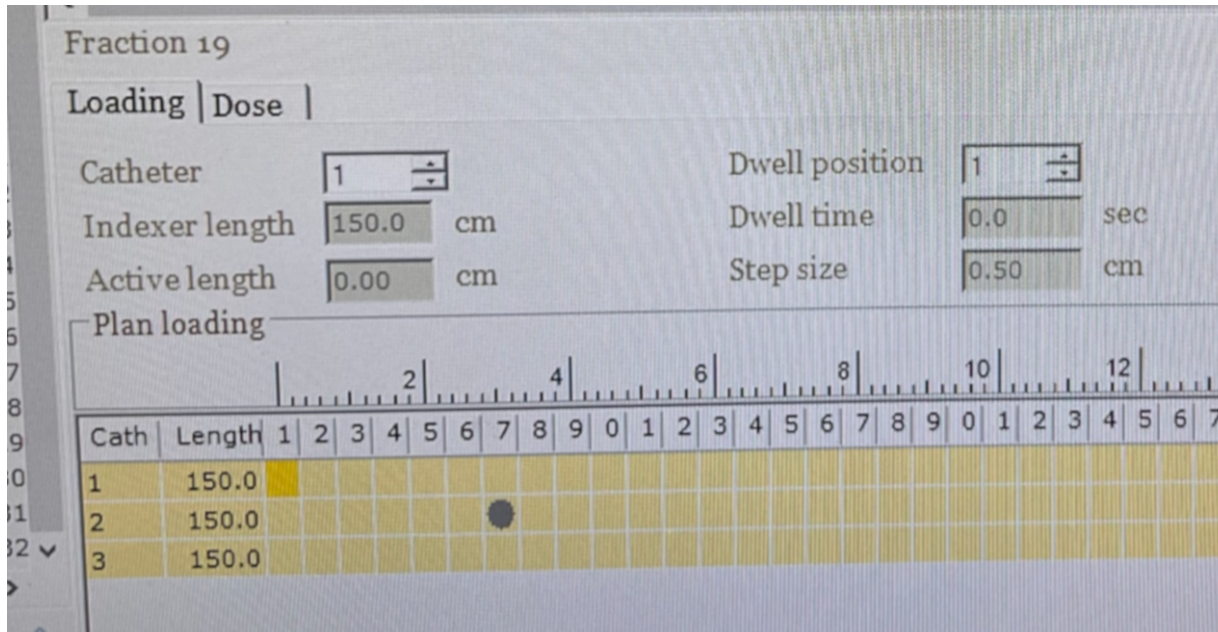


Figure 36: Treatment delivery system view of the single dwell position for the depth dose plan.

2.4. Egs_brachy modeling

The Monte Carlo package used to run the simulations was the egs_brachy package provided with the EGSnrc (national research council) code. The egs_brachy code is specific to brachytherapy simulations, there are other packages available for other simulation scenarios (external beam, ion chambers etc). In egs_brachy there are several prepared materials, sources, geometries, and spectra among other items that may be used for modeling. For this work, a simple custom geometry was created using water, the provided SS_AISI316L_p8.02 stainless steel material, and the Elekta MicroSelectron Ir-192 source and spectrum. The stainless steel was also used in Semeniuk *et al.* along with another, less dense, stainless steel material. The two samples showed near identical shielding properties [30]. The geometry was contained in a 30 cm water cube, with a scoring region of a 10 cm cube of water with a 5 cm x 5 cm piece of steel with varying thickness. The steel was placed with the same geometry as the film measurements, with the furthest side of the metal placed

at 1 cm from the source. The steel used has a density of 8.02 g/cm^3 which is slightly higher than the density of the metal samples used (average density 7.2 g/cm^3), which would be expected to show similar patterns at a higher shielding capacity (on the order of 10% difference). The source was oriented so the anisotropy that occurs at the tip was not directed at the metal (Figure 38), which matches the orientation that was used when taking the depth dose measurements using film. The simulation was run using $2e8$ histories, and each particle was recycled 6 times in order to achieve an error $<5\%$ in the entire scoring area in a reasonable run time. The dose deposition was measured in the scoring region and was used for analysis.

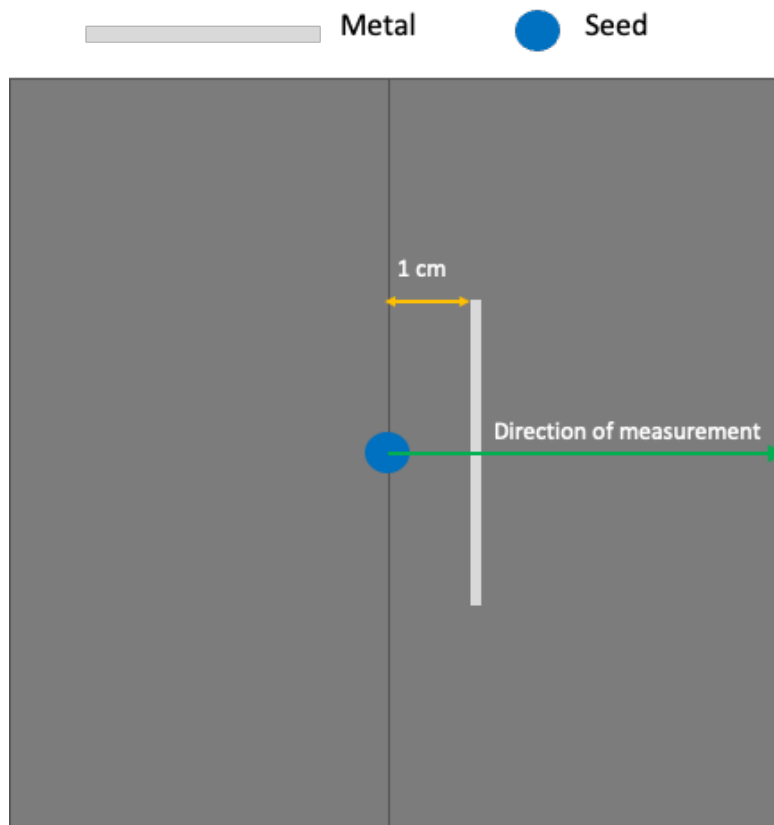


Figure 37: Graphic of the egs_brachy phantom.

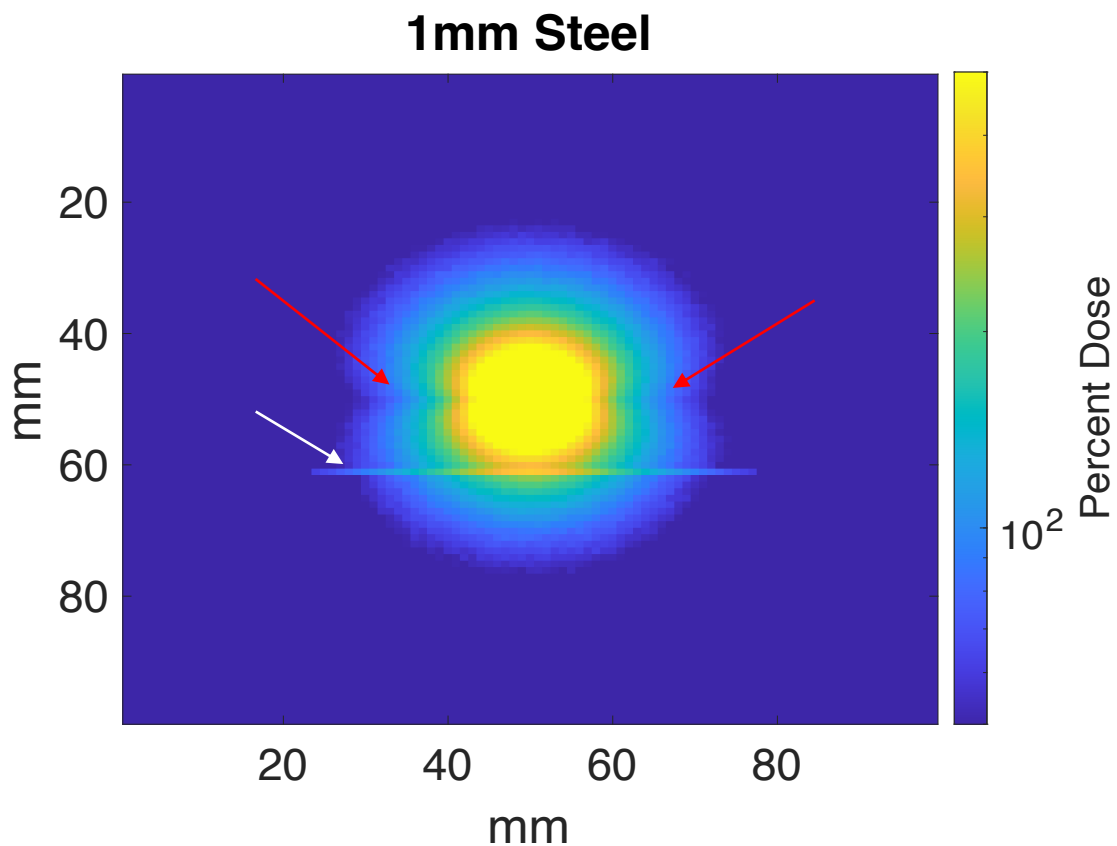


Figure 38: egs_brachy dose reading, showing the anisotropy of the single seed at the center (red arrows) relative to the plane of the metal (white arrow). The maximum value for the colour scale is 500% dose. Since the metal is denser than the surrounding water, it shows a higher dose deposition

3. Results

3.1. Film

3.1.1. Calibration Curve

The calibration films were exposed at a dose range of 100 cGy to 400 cGy with 50 cGy increments and including an unexposed piece of film at 0 cGy. The scanned images of the film were imported into the software FilmQAPro, which is capable of fitting the calibration curves as well as analysing dose from film using the given calibration curve. The three-colour channel calibration curves are shown in Figure 39. All three calibration curves produce similar results when used, but due to the steeper slope in the red channel, it was chosen for continued calibration purposes. The steeper slope means that the range of colours in the film used for the different dose values is greater, resulting in a greater sensitivity. To limit any error coming from the calibration process only the red curve was used, though no major discrepancies were noted between the channels. The red channel has been used by itself or in conjunction with other channels and has been shown to be the most sensitive of the three colour channels [27], [51]–[53].

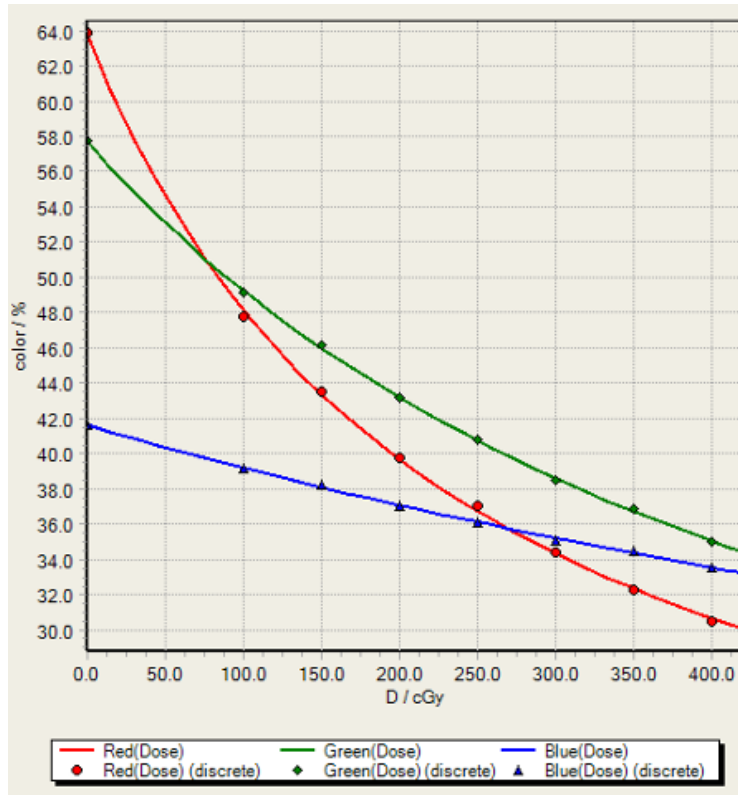


Figure 39: Calibration curves of the film

3.1.2. Planar

The dose reading for 200 cGy delivered to the film in only solid water was measured to be 202.5 cGy, which gave a calibration error on the order of 1%. Once the calibration curve was corrected, the test films were read. The dose delivered to the film with no metal present was normalized to be 100% dose. The rest of the film were normalized with this value, as a percent of the dose delivered only in water. The error displayed is 7.5% error of the film measurement and is detailed in Table 3. The values are shown below in Figure 40, with a minimum of $3.9 \pm 7.1\%$ shielding (1 mm of metal directly adjacent to the film) and a maximum of $26.5 \pm 5.5\%$ shielding (5 mm of metal at the midpoint). The values were measured in a 2.5 mm square, centered on the pixel with the highest dose value.

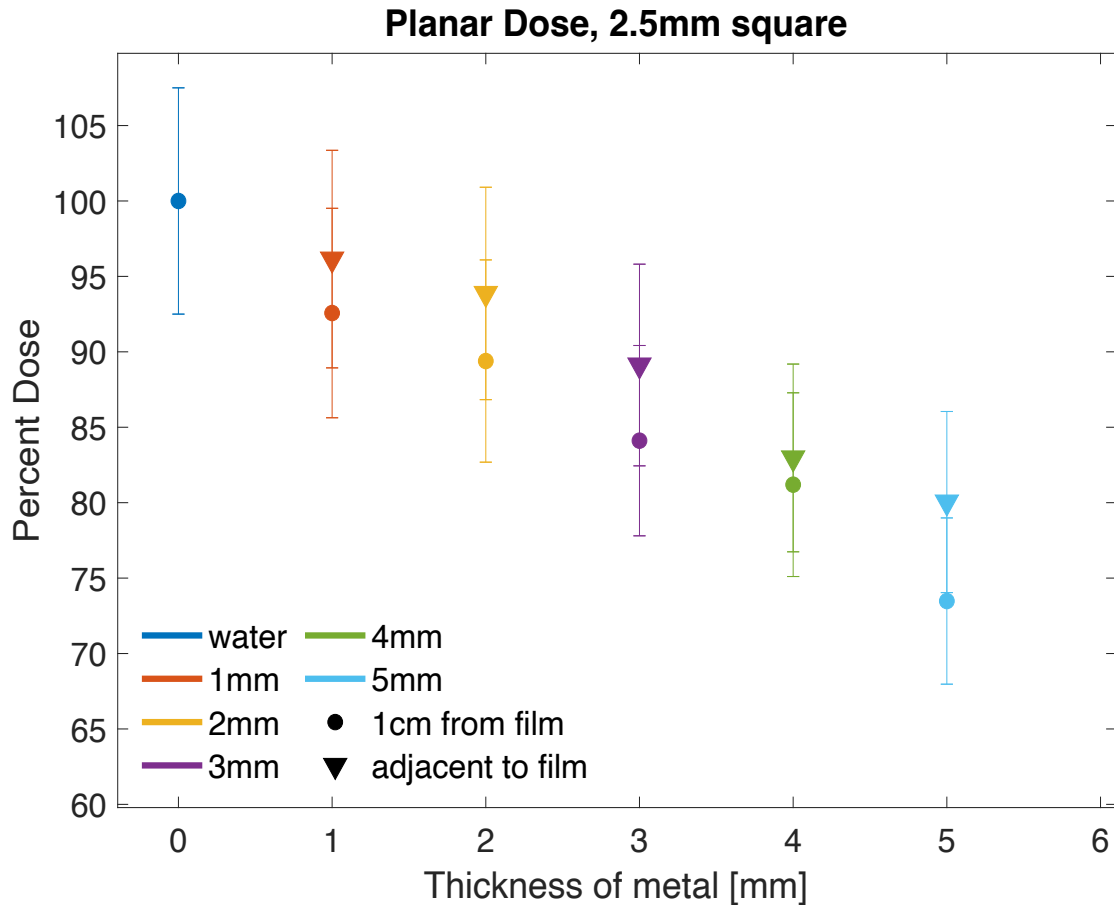


Figure 40: Planar percent dose delivered in water, measured using the red calibration channel. The values using the setup with the metal halfway between the catheters and the film are shown with a circle, and the values from the setup where the metal is directly adjacent to the film are shown with a triangle. The error displayed is 7.5% error on the film measurement, detailed in Table 3

3.1.3. Data Validation

To determine if the simulation results and the film results were behaving as expected, the depth dose curves measured without metal were compared to a $1/r^2$ decay curve (expected decay of radiation without attenuation and scatter) and the dose values

calculated from the depth dose plan in Oncentra. The shape of all of the depth dose curves agree within error, allowing for comparison between them.

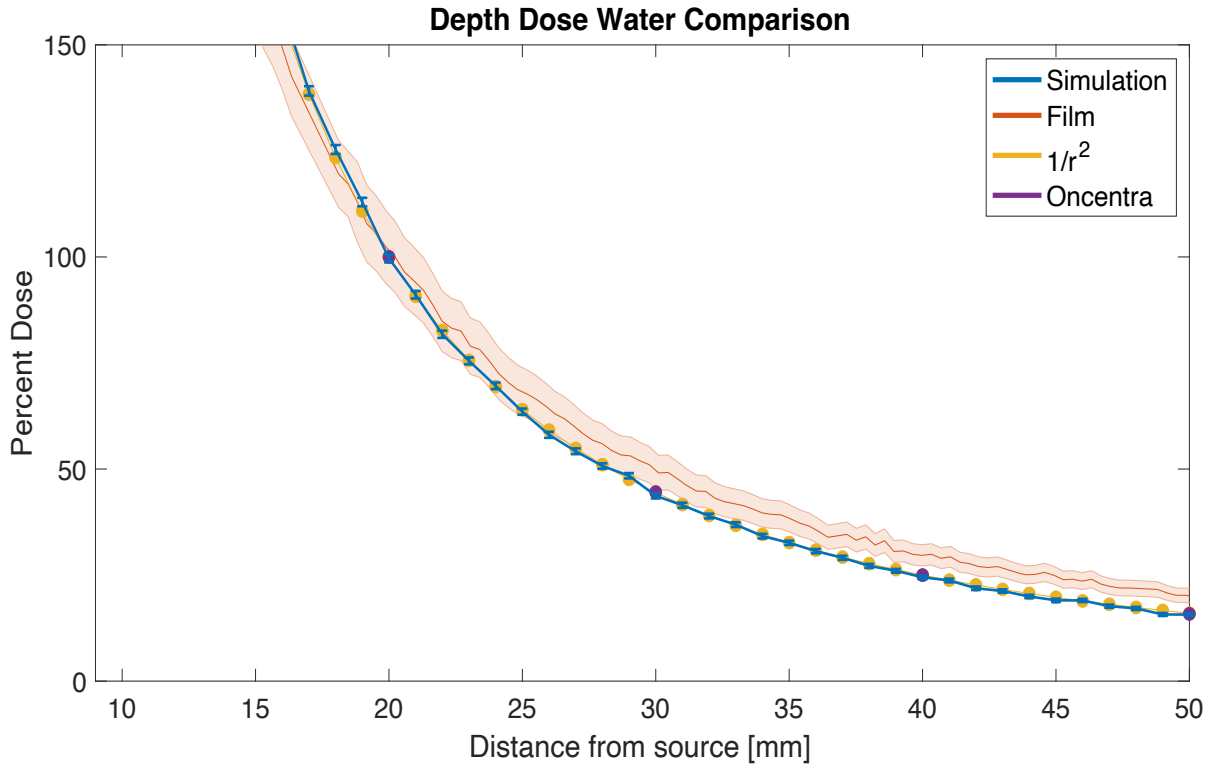


Figure 41: A comparison of different depth dose in water using *egs_brachy*, film, the Oncentra planning system, and the expected decay of $1/r^2$. Shaded area around the film curve shows the error of the film measurements.

3.1.4. Depth Dose

These films were all scanned in the same batch after the initial calibration curve, so they also required calibration correction films. These were taken at 0 cGy and 400 cGy and a test of 200 cGy was taken as well (these measurements are all taken in the planar orientation with the planar plan without any metal present). The 200 cGy test was measured at 196.0 cGy, which is a calibration error of 2%. To find the area on the film to measure the depth dose, the maximum value was found 15 pixels from the edge of the

film and then a width of 2.5 cm (7 pixels) was averaged to create the depth dose data. The dose delivered in water only was used to normalize the film, the point at 2 cm from the source was set to 100% dose. Due to separation at the edge of the film which occurs every time it is cut, the first 10 mm were disregarded, and to better see the shape of the curves, values are plotted to a limit of 150% (Figure 42). The relative dose difference is also plotted along the depth and shows a maximum of $21.1 \pm 5.3\%$ shielding. (Figure 43). The thin pieces of solid water were used to fill the air gaps under the metal samples that were thinner than 5 mm, and the solid water that held up the film were taped together to keep them together.

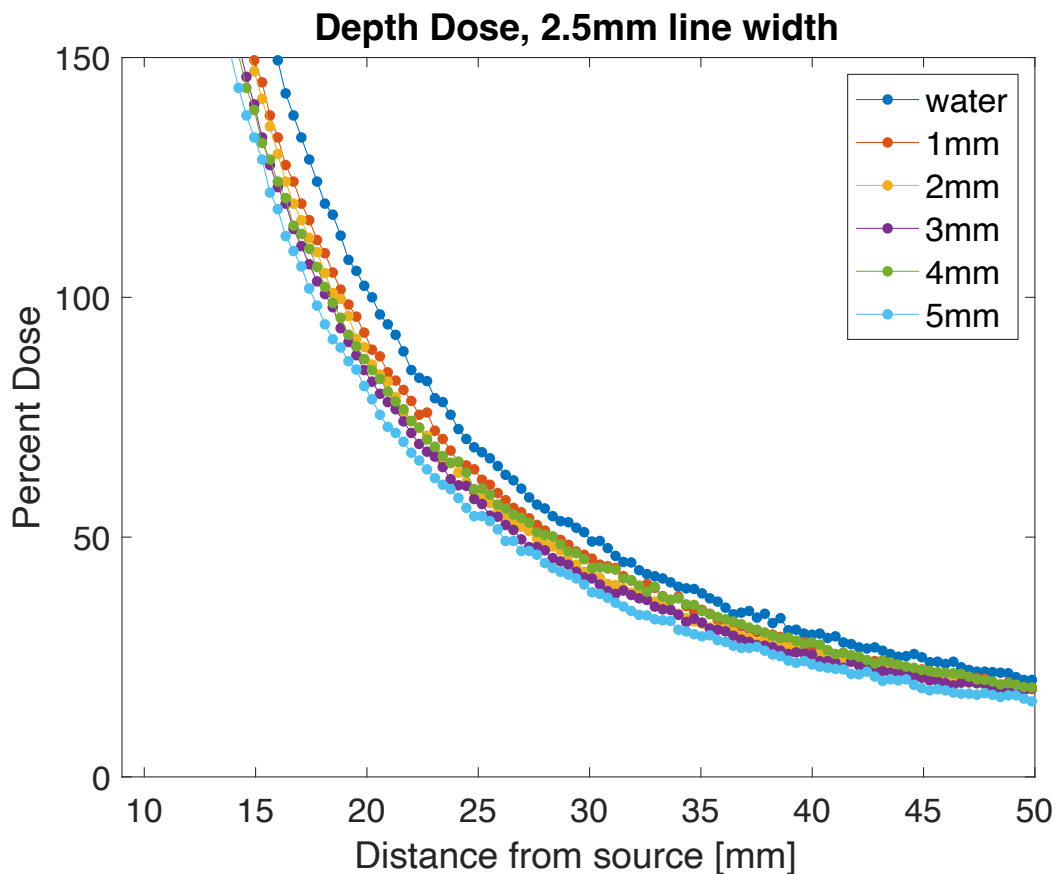


Figure 42: The depth dose measured with film using varying thicknesses of metal ranging from 0 mm to 5 mm.

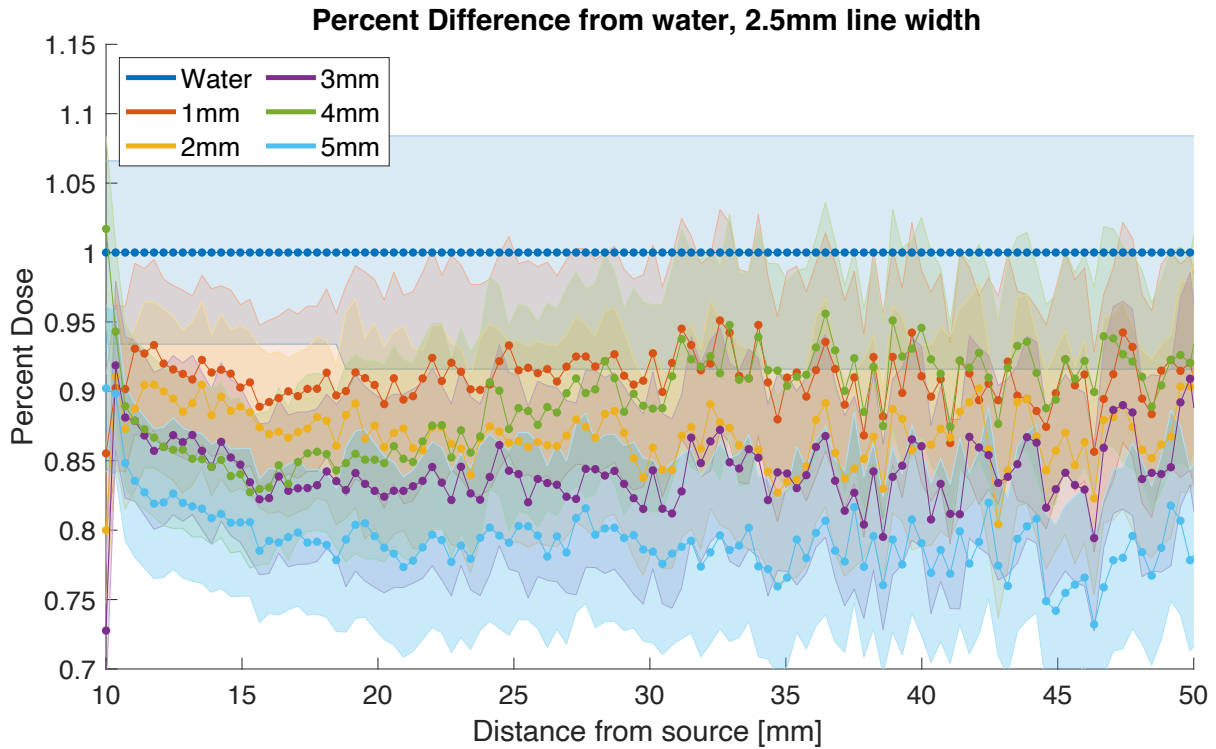


Figure 43: The percent difference from water measured using film. The metal thicknesses range from 1 mm to 5 mm. The error from the film measurements is shown as the shaded region.

3.2. Egs_brachy

Using egs_brachy to simulate a single Ir-192 seed and varying thicknesses of metal the following data was collected. The figures below follow the same axes as above. The region around 10 mm shows some dose enhancement due to its proximity to the steel. To find the area of the produced data to average for the depth dose, the central pixel and the two pixels on either side were averaged (3 pixels are 3 mm wide). The point 2 cm from the source when only water was present was used as the normalization point and was set to 100% dose. 5 mm of steel provided $16.3 \pm 0.9\%$ shielding. 10 mm of steel provided approximately 30% shielding (Figure 45).

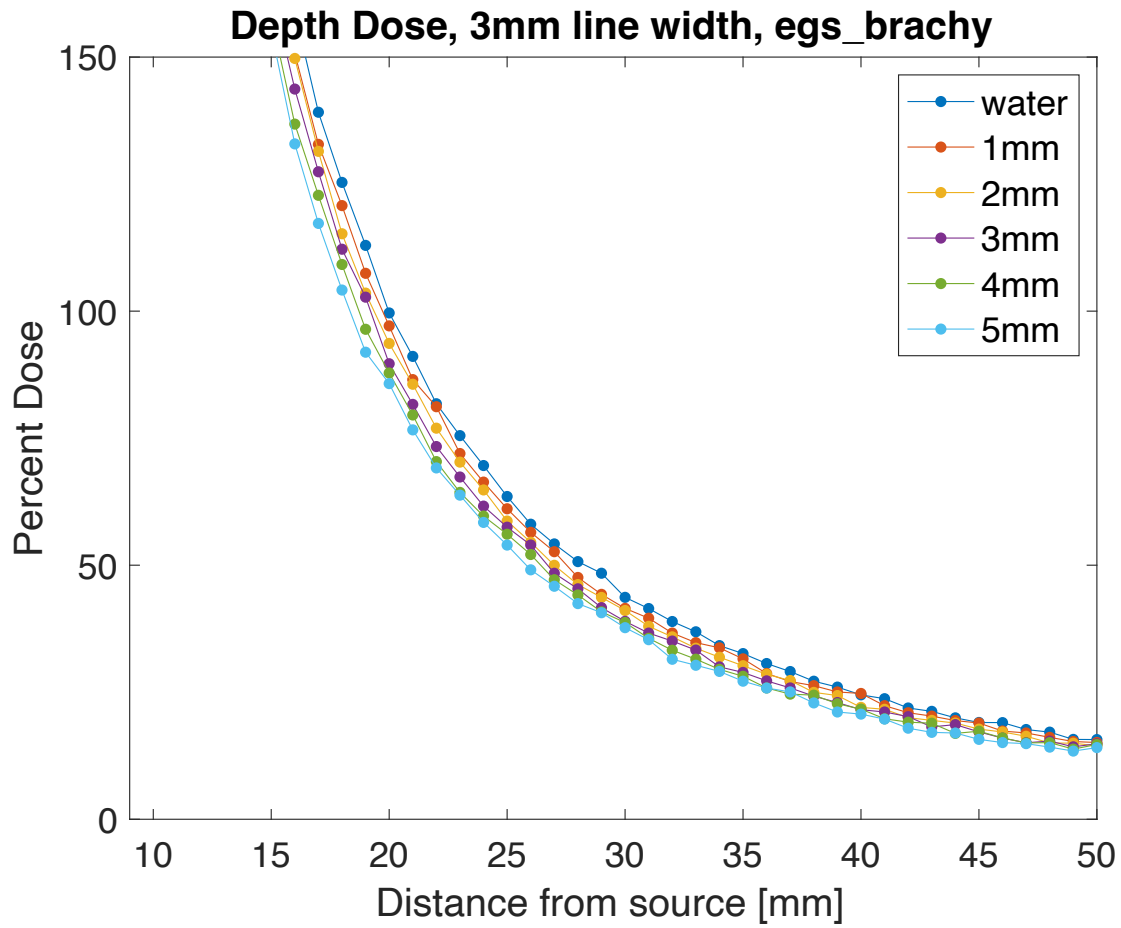


Figure 44: Depth dose measured using `eggs_brachy` simulations. The thickness of metal simulated range from 1 mm to 5 mm.

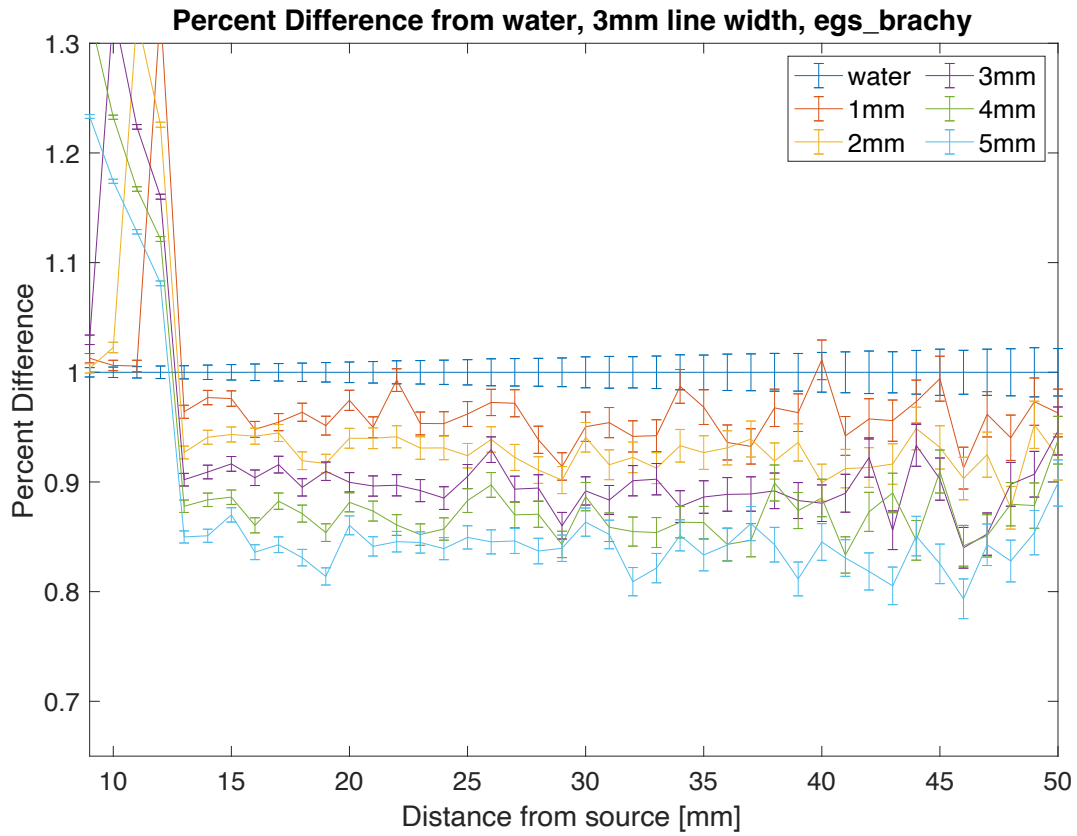


Figure 45: Percent difference measured using `egs_brachy` simulations. The metal thicknesses range from 1 mm to 5mm.

4. Discussion

4.1. Uncertainty Analysis

The uncertainty for the egs_brachy simulation is determined from the simulation itself. The uncertainty analysis for the film is taken from Oare *et al.*, which is influenced by the suggested method from TG-43. The intention of Oare *et al.* was to determine any dose differences and uncertainties for 3D printed water equivalent applicators for brachytherapy. The underlined descriptions in Table 3 are values that are the same from Oare *et al.*, as the same type of film and source were used. The ROI size used in this work is included in the range for 1.5% error [27]. The distance to source error was calculated using the $1/r^2$ principle using a 1 mm shift for the planar dose measurements and a 2 mm shift for the depth dose measurement [27]. Due to possible positioning errors a 2 mm shift was chosen for the depth dose measurement error, and due to the potential variation in metal thickness which would leave air gaps a “shift” of 1 mm is chosen as error for planar dose measurements. The exposure time used the same error of 0.4 seconds from Oare *et al.* but used the time that it took for 200 cGy to be exposed (~90s) for that calculation [27]. The calibration curve fit comes from the discrepancy between 200 cGy and the test piece of film used to check the corrected calibration used for dosimetry. All the film had a 3% error on the corrected calibration. The total errors in the table below show the error displayed in the film measurements in the shaded regions of the figures.

Table 3: Description and value of uncertainties, using the method of Oare et al. The underlined descriptions are values that are the same from Oare et al., as the same conditions were met.

Uncertainty Description	Value
<u>Scanning consistency</u>	0.1 %
<u>Film uniformity</u>	1.0 %
ROI size	1.5 %
Calibration Curve Fit	3.0 %, 6.0% (low dose, depth dose only)
<u>Repeatability</u>	0.1 %
Distance to source	4.0 % (planar), 2.0% (depth dose)
<u>Lack of scatter equilibrium</u>	5.0%
<u>Source Strength</u>	1.5%
Exposure Time	0.4%
Total	7.5% (planar), 6.6% (depth dose), 8.4% (depth dose, low energy)

4.2. Planar

The planar dose delivery plan includes several different seed positions and angles traveling through the metal (Figure 46). This is most similar to how a patient would be treated (instead of a single seed position). As the thickness of metal increases, the dose deposited past the metal decreases. This aligns with what was expected, with a quantification of the decrease. There is also an increase in dose when you measure directly adjacent to the metal, which is seen in the planar measurements (Figure 40), implying that there is some dose enhancement effects present when the metal is irradiated. This is not an unexpected outcome, as when metal is irradiated some electrons are produced, due to the photoelectric effect and Compton scattering, which would increase the dose in the most immediate tissue [17].

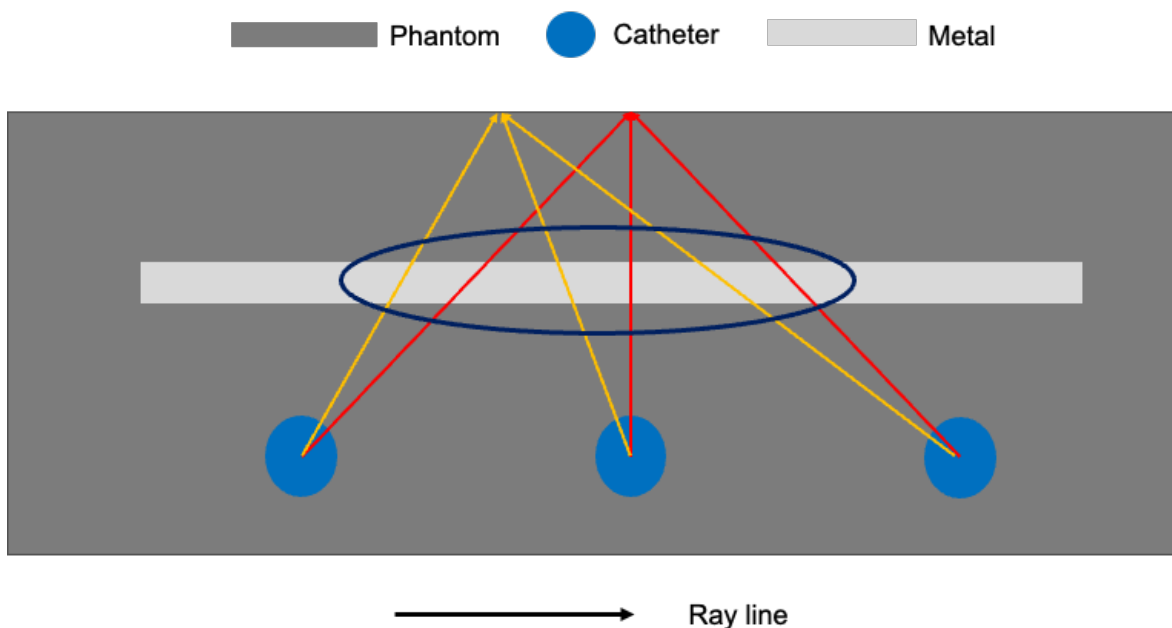


Figure 46: Graphic demonstration of the different path lengths through the metal with multiple source positions, the circled region highlights where these differences lie

The decrease in dose as the thickness increases is generally consistent, with an average decrease of 5.3% dose/mm of steel for the planar measurements taken 2 cm from the plane of the catheters. The planar measurements are an average of a 2.5 mm square centered on the maximum pixel value found in area of dose delivery. There are some larger differences, namely from 0 mm to 1 mm, and 4 mm to 5 mm when the metal was midway between the catheters and the film, these had an average dose decrease of 7.5%. The same fluctuation is not seen in the measurements from the film that is directly adjacent to the metal, and these values decreased an average of 4.0% dose/mm of steel.

The 5 cm x 5 cm x 5 mm piece of steel weighed 116 g, which when compared to the same volume of water (12.5 g) is a considerable increase in weight. Depending on the size of the area that is intended to be shielded, there may be even more steel present in a 3D printed applicator. This may affect the comfort and ease of use of the applicator, while only

providing between 20% and 26% shielding. The effectiveness of this specific material may not be ideal for total shielding but would be able to provide partial shielding or improved dose modulation. The rectum, bladder, urethra, colon, sigmoid, and vaginal wall and mucosa are nearby organs that are considered when creating treatment plans for vaginal brachytherapy [7], [30], [33], [54], [55]. One work found the mean dose to some of these organs using a conventional single-channel cylinder [56]. The doses were: bladder $23.7 \pm 8.8\%/35.7 \pm 13.3$, rectum $24.6 \pm 5.6\%/37.2 \pm 8.6\%$, sigmoid $15.2 \pm 7.6\%/24.2 \pm 12.3\%$, urethra $24.1 \pm 12.2\%/36.4 \pm 16.5\%$, as percent prescription dose at the surface of the applicator and at a 0.5 cm depth from the applicator surface [56]. This was achieved with a water equivalent applicator, so the presence of shielding using the same dose delivery plan could allow for reduced dose to these nearby organs while providing the same dose to the target volume. Using the same treatment plan, the inclusion of steel could decrease the dose to these organs further but would not be able to provide full shielding.

The Semeniuk *et al.* work investigated theoretical 3D printed gynecological brachytherapy designs based on the applicator described in TG-186. The applicator has a diameter of 3.6 cm, with a central channel diameter of 3.2 mm (central 1 mm is an air channel for a catheter and the surrounding 2.2 mm are made of stainless steel) [30]. This leaves a maximum 1.64 cm for shielding material thickness, and to achieve sterilizability the portion in contact with tissue must be the same material for sterilizing purposes so in reality the thickness will be less than 1.64 cm. The Skinner *et al.* work uses an applicator design that is 30 mm in diameter and features a Miami style applicator with a central catheter channel and more channels distributed radially. This design allows for a maximum thickness of less than 15 mm, which is consistent with Semeniuk *et al.*

Extrapolating from Figure 40, 15 mm of stainless steel would provide approximately 70% shielding. Semeniuk *et al.* finds that WPLA is able to provide approximately 80% shielding. Skinner *et al.* finds that, using a Miami style applicator, they are able to achieve between 40% and 50% shielding, but they intend to print applicators using the denser material WPLA. WPLA has a density of 9 g/cm³ and the stainless steel used in this work has a density of approximately 7.2 g/cm³, but WPLA has a much higher mass attenuation coefficient (WPLA 0.2130 cm²/g, stainless steel 0.0979 cm²/g for 380 keV photons) [30].

4.3. Depth Dose

Cunha *et al.* showed that film could be used to determine water equivalency of a material. A custom apparatus was printed using PC-ISO and was printed to hold a piece of film and a catheter [26]. The film was held so it was perpendicular to the catheter and able to capture the depth dose measurement through PC-ISO [26]. The dose plan used to deliver the radiation had dwell positions along the length of the apparatus [26]. The film was exposed in the PC-ISO apparatus and while it was submerged in water, the results were compared and were found to be within 1% of each other [26].

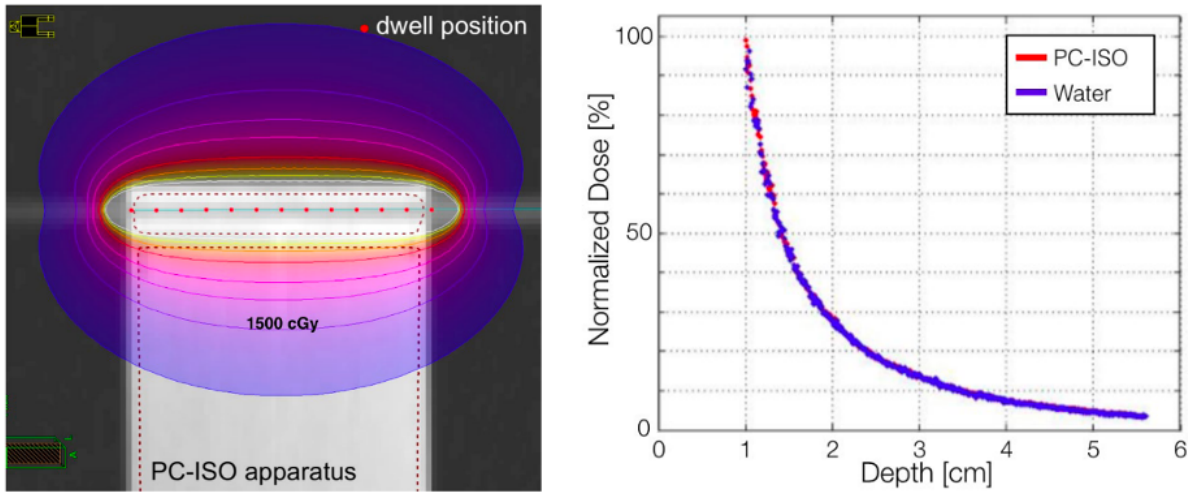


Figure 47: Left: dose delivery plan used by Cunha *et al.*, Right: the resulting percent depth dose curves through water and PC-ISO [26]

The water measurements from Figure 41 show that the simulation and film measurements are comparable, at least until 40 mm from the source. Oare *et al.* discusses the error found when using film for dosimetry, and that the error increase for EBT3 film at low doses primarily due to a decreased signal to noise ratio, which they determined was 100 cGy and below [51]. The film used reaches 100 cGy between 25 and 30 mm from the source, depending on the thickness of metal present. Therefore, the error values increase past this distance to account for the accuracy of the film at lower doses [27].

The simulation and film results agree within error (simulation $16.3 \pm 0.9\%$ and film $21.1 \pm 5.3\%$, for 5 mm of steel), and both show the expected increase in shielding as the thickness increases. They also show that the shielding is maintained as the distance from the source increases. These results show nominal shielding capabilities to be lower than the planar results but appear to more closely agree with the planar measurements taken directly adjacent to the metal ($20.0 \pm 6.0\%$ adjacent for 5 mm of steel). A Wilcoxon-Rank test was performed on the two data sets and found that there was a difference between the two, but

that the difference was not statistically significant except for the measurements taken with 3 mm of steel. Since the depth dose measurements are also taken with direct contact with the metal this shows consistency of potential dose enhancement between the measurement methods. Using Monte Carlo simulations, a projection at 10 mm thickness was calculated and resulted in a predicted 30% shielding to be achieved with that thickness.

Semeniuk *et al.* and Skinner *et al.* both use multiple source dwell positions. As before, due to the range of angles through the shielding material that occurs with multiple dwell positions the shielding capabilities will not necessarily match the shielding that is measured from a single dwell position. This causes the shielding capabilities measured with multiple dwell positions to be difficult to compare with shielding measured with only one dwell position because the radiation conditions and paths through the shielding conditions differ.

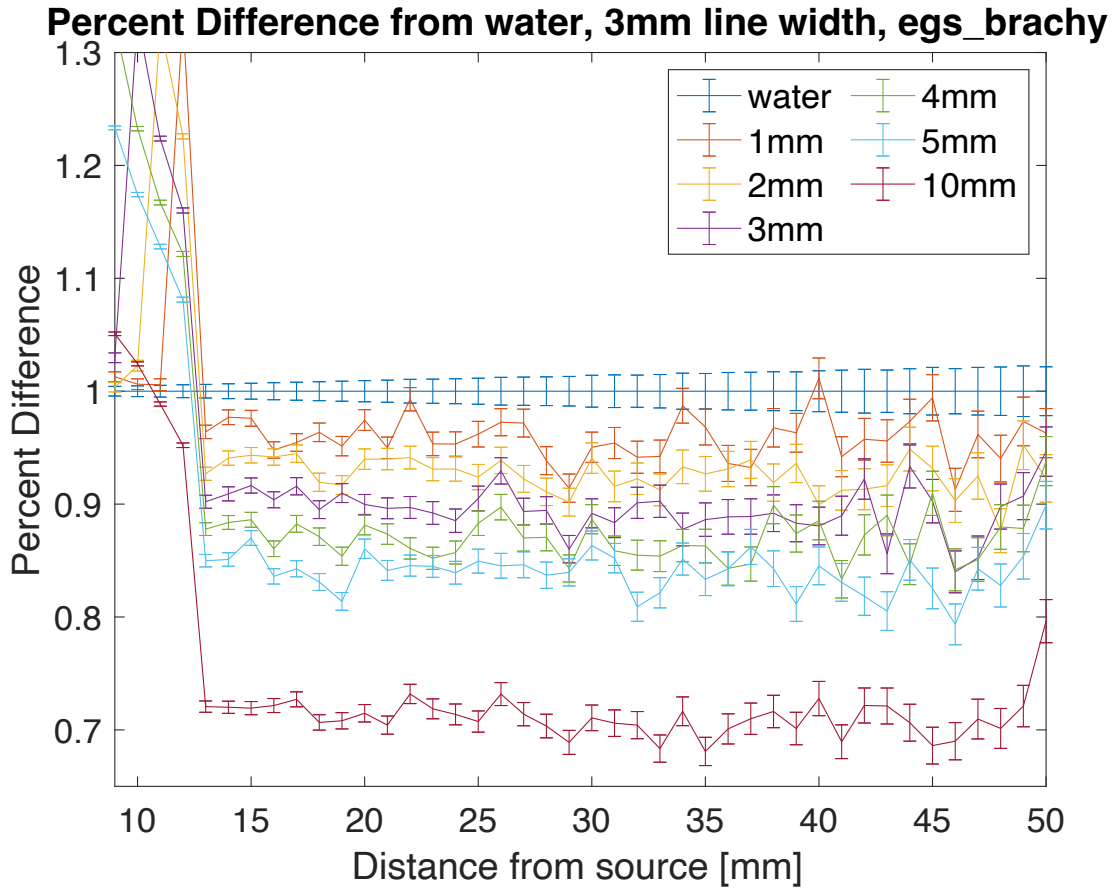


Figure 48: Percent difference from water, including 10 mm thickness of steel, done using eggs_brachy

5. Conclusion

5.1. Summary of work

This work sought to characterize the shielding capabilities of stainless steel samples as a means for brachytherapy treatment with 3D printed applicators. Radiochromic film was used to measure the shielding capabilities of a range of metal thicknesses (1 mm to 5 mm). The measurements were taken in two geometries (planar and depth dose) with three variations. Planar measurements were taken with the film parallel to the plane of the catheters and the metal in two different positions relative to the film (adjacent and 1 cm away). The treatment plan used had many seed positions and dwell times that created an isodose area in the plane of the film. Depth dose measurements were taken with the film perpendicular to the plane of the catheters and one position for the metal. The film was exposed using a single dwell position to capture depth dose from a single direction. A Monte Carlo simulation was created using the EGSnrc program `egs_brachy` and the geometry was created to emulate the depth dose measurement geometry. 5 mm of steel in the planar orientation was found to provide $26.5 \pm 5.5\%$ shielding when the metal was 1 cm away from the film, and $20.0 \pm 6\%$ shielding when the metal was directly adjacent to the film. 5 mm of steel in the depth dose orientation provided $21.1 \pm 5.3\%$ shielding when measured with film and $16.3 \pm 0.9\%$ shielding when simulated using `egs_brachy`. An increase in thickness to 10 mm increases the shielding to $\sim 30\%$ when simulated.

The stainless steel is able to provide shielding, but the shielding values are not significant when considering the additional time and workload needed to produce a personalized applicator. To improve the shielding capabilities more metal would need to be used and the thickness is limited to the size of the applicator being used. Stainless steel is

also fairly heavy, and an applicator made using the Semeniuk *et al.* theoretical model would weigh on the order of several kilograms. To provide shielding without so much weight, a higher density material would be preferable.

5.2. Future work

In future works, this method can be used to assess different materials for their shielding capabilities. Materials likely to show higher shielding capabilities would be those with a higher density, like tungsten which has been mixed with 3D printing material previously as a potential shielding material [30], [34]. There is also the newer technique where metal is able to be printed itself without the need to mix it with existing 3D printing plastic [29]. There are currently techniques to 3D print with powdered metal directly, which would remove the need to mix powdered metal with a 3D printing plastic. The new HP Metal Jet technology allows for metal to be printed directly in layers and subsequently sintered together to form a solid piece of metal in the desired shape [29]. Post processing may be used to achieve the desired finish on the piece, but this method allows for metal to be printed with layers of 35 to 140 microns in thickness [29].

Depth dose measurements agree with each other, but do not agree with the planar measurement. This is most likely due to the difference in source positions and angles through the metal, causing different path lengths of radiation and therefore a range of different expected shielding capabilities. Using the simulation data that we have corroborated with the film in this work, a future experiment could create the dwell positions from the planar dose delivery plan in the `egs_brachy` software and then compare the results of that simulation with the results from the film measurements. The seeds could all be placed inside one phantom

and simulated all at once, or each dwell position could be simulated individually and then the dose distributions could all be added together. Should the dose distributions match the ones measured with film, this would allow greater insight into the differences between the depth dose measurements and the planar measurements, given that the simulations do not require physical measurements. The differences could be compared more directly, with the myriad of distances and angles that may be simulated.

With the ability to 3D print in mind, a model could be printed and tested as well with a modified methodology to gauge the dose distribution in a realistic applicator. These could also be compared with simulated data to match and could be used to create a method for choosing shielded areas in personalized applicators in future [30], [34]. Using the patient's anatomy and geometry, the system could include many other factors when selecting shielding areas such as nearby tissue sparing, and the additional weight to the applicator for the shielding to be achieved.

The potential workflow outlined in Semeniuk *et al.* would be one that could function with any shielded 3D printed applicator. A CT or MRI image would be required for contouring and then for simulations. A Monte Carlo simulation, or other MBDCA (such as a grid-based Boltzmann equation solver, or a collapsed cone superposition/convolution method) would be used for dose and shielding calculation especially if personalized shielding is being implemented [50]. A personalized applicator with shielding will require phases of design. The area intended for treatment should maximise dose delivery, while areas that do not overlap but contain nearby organs may include shielding. Given the prescription from the radiation oncologists, the dose distribution and dose volume histograms can be used to create an applicator that provides the required dose to the target and shielding to specified organs.

Then the designed applicator will be printed, and quality testing should be performed to ensure no errors occurred in the printing process. Final imaging should be taken, either with a dummy piece inserted instead of shielding or the shielding material will ideally be MRI/CT compatible.

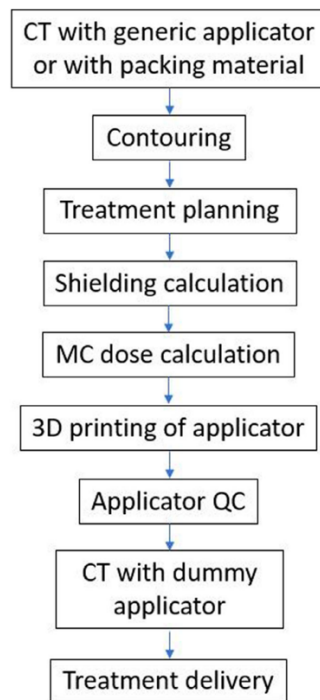


Figure 49: Potential workflow outlined in Semeniuk et al.

This work focuses on the design of gynecological applicators, where there are many nearby organs at risk which would benefit from increased shielding during treatment. The applicator itself is where the shielding is included, so there is not an extra piece of equipment for shielding. Rectal brachytherapy with a cylindrical applicator may benefit from the same shielding described in this work. 3D printed superficial applicators may also benefit from the inclusion of shielding material, to prevent the spread of dose to lateral areas of normal tissue. Generalising the method for providing shielding, a 3D printed applicator for brachytherapy treatment could include shielding to provide additional shaping to the dose distribution.

Bibliography

- [1] B. L. Hoffman, J. O. Schorge, L. M. Halvorson, C. A. Hamid, M. M. Corton, and J. I. Schaffer, "Principles of Radiation Therapy," in *Williams Gynecology, 4e*, New York, NY: McGraw-Hill Education, 2020. [Online]. Available: <http://accessmedicine.mhmedical.com/content.aspx?aid=1171532575>
- [2] K. Albuquerque, S. Beriwal, A. N. Viswanathan, and B. Erickson, *A Comprehensive Practical Guide Practical Guides in Radiation Oncology*. 2019. [Online]. Available: <http://www.springer.com/series/13580>
- [3] "Cancer types | Canadian Cancer Society." <https://cancer.ca/en/cancer-information/cancer-types> (accessed Jul. 05, 2023).
- [4] M. Jreij, A. El Ahmar, and P. Finianos, "Applicators used for vaginal high dose rate brachytherapy: Effect of type and shape on dose distribution and toxicity, a literature review," *Cancer/Radiotherapie*, vol. 27, no. 1, pp. 80–85, 2023, doi: 10.1016/j.canrad.2021.10.013.
- [5] M. J. Rivard *et al.*, "Update of AAPM Task Group No. 43 Report: A revised AAPM protocol for brachytherapy dose calculations," *Med Phys*, vol. 31, no. 3, pp. 633–674, Mar. 2004, doi: 10.1118/1.1646040.
- [6] X. Wu *et al.*, "Dose Optimization for Single-Channel Vaginal Cylinder High-Dose-Rate Brachytherapy: A Double Prescription Method for Patients With Endometrial Adenocarcinoma," *Cureus*, vol. 14, no. 6, Jun. 2022, doi: 10.7759/CUREUS.26303.
- [7] Y. A. Bahadur, C. Constantinescu, A. H. Hassouna, M. M. Eltaher, N. M. Ghassal, and N. A. Awad, "Single versus multichannel applicator in high-dose-rate vaginal brachytherapy optimized by inverse treatment planning," *J Contemp Brachytherapy*, vol. 6, no. 4, pp. 362–370, 2014, doi: 10.5114/jcb.2014.47816.
- [8] W. Small *et al.*, "American Brachytherapy Society consensus guidelines for adjuvant vaginal cuff brachytherapy after hysterectomy", doi: 10.1016/j.brachy.2011.08.005.
- [9] Y. A. Bahadur, C. Constantinescu, A. H. Hassouna, M. M. Eltaher, N. M. Ghassal, and N. A. Awad, "Single versus multichannel applicator in high-dose-rate vaginal brachytherapy optimized by inverse treatment planning," *J Contemp Brachytherapy*, vol. 6, no. 4, p. 362, 2015, doi: 10.5114/JCB.2014.47816.
- [10] M. Serban *et al.*, "Ring Versus Ovoids and Intracavitary Versus Intracavitary-Interstitial Applicators in Cervical Cancer Brachytherapy: Results From the EMBRACE I Study," *Int J Radiat Oncol Biol Phys*, vol. 106, no. 5, pp. 1052–1062, 2020, doi: 10.1016/j.ijrobp.2019.12.019.
- [11] A. Mourya, L. Aggarwal, and S. Choudhary, "Evolution of Brachytherapy Applicators for the Treatment of Cervical Cancer," *J Med Phys*, vol. 46, no. 4, p. 231, Oct. 2021, doi: 10.4103/JMP.JMP_62_21.
- [12] "Rectum | Brachytherapy | Radiotherapy Treatment | Elekta." <https://www.elekta.com/products/brachytherapy/rectum/> (accessed Aug. 24, 2023).
- [13] C. W. Colvin and H. Abdullatif, "Anatomy of female puberty: The clinical relevance of developmental changes in the reproductive system," *Clinical Anatomy*, vol. 26, no. 1, pp. 115–129, Jan. 2013, doi: 10.1002/CA.22164.
- [14] M. Bakhshabadi, M. Ghorbani, M. Khosroabadi, C. Knaup, and A. S. Meigooni, "Physics Contributions A comparison study on various low energy sources in interstitial prostate brachytherapy," *J Contemp Brachytherapy*, vol. 8, no. 1, pp. 74–81, 2016, doi: 10.5114/jcb.2016.57708.

- [15] M. Ghorbani, A. Mozaffari, and H. Akbari-Lalimi, “Presentation of a matrix-based method to calculate dose distribution in brachytherapy with photon-emitting sources,” *J Cancer Res Ther*, vol. 15, no. 6, pp. 1245–1253, Oct. 2019, doi: 10.4103/jcrt.JCRT_1274_16.
- [16] P. Andreo *et al.*, *Radiation Oncology Physics: A Handbook for Teachers and Students*, vol. 52, no. 20. 2004. doi: 10.1021/jf030837o.
- [17] F. H. ATTIX, *INTRODUCTION TO RADIOLOGICAL PHYSICS AND RADIATION DOSIMETRY*. 1986. Accessed: Jul. 26, 2023. [Online]. Available: <http://dnb.ddb.de>
- [18] M. J. Rivard *et al.*, “Supplement to the 2004 update of the AAPM Task Group No. 43 Report,” *Med Phys*, vol. 34, no. 6, pp. 2187–2205, 2007, doi: 10.1118/1.2736790.
- [19] M. J. Rivard *et al.*, “Supplement 2 for the 2004 update of the AAPM Task Group No. 43 Report: Joint recommendations by the AAPM and GEC-ESTRO: Joint,” *Med Phys*, vol. 44, no. 9, pp. e297–e338, Sep. 2017, doi: 10.1002/MP.12430.
- [20] L. Beaulieu *et al.*, “Report of the Task Group 186 on model-based dose calculation methods in brachytherapy beyond the TG-43 formalism: Current status and recommendations for clinical implementation,” *Med Phys*, vol. 39, no. 10, pp. 6208–6236, Oct. 2012, doi: 10.1118/1.4747264.
- [21] L. Beaulieu *et al.*, “Report of the Task Group 186 on model-based dose calculation methods in brachytherapy beyond the TG-43 formalism: Current status and recommendations for clinical implementation,” *Med Phys*, vol. 39, no. 10, pp. 6208–6236, 2012, doi: 10.1118/1.4747264.
- [22] A. L. Palmer *et al.*, “Comparison of methods for the measurement of radiation dose distributions in high dose rate (HDR) brachytherapy: Ge-doped optical fiber, EBT3 Gafchromic film, and PRESAGE® radiochromic plastic,” *Med Phys*, vol. 40, no. 6Part1, p. 061707, Jun. 2013, doi: 10.1118/1.4805100.
- [23] “GAFCHROMIC™ DOSIMETRY MEDIA, TYPE EBT-3”, Accessed: Jul. 23, 2023. [Online]. Available: www.FilmQAPro.com.
- [24] A. L. Palmer, D. Bradley, and A. Nisbet, “Evaluation and implementation of triple-channel radiochromic film dosimetry in brachytherapy; Evaluation and implementation of triple-channel radiochromic film dosimetry in brachytherapy,” *J Appl Clin Med Phys*, vol. 15, no. 4, 2014, doi: 10.1120/jacmp.v15i4.4854.
- [25] “Efficient Protocols for Accurate Radiochromic Film Calibration and Dosimetry”.
- [26] J. A. M. Cunha *et al.*, “Evaluation of PC-ISO for customized, 3D printed, gynecologic 192Ir HDR brachytherapy applicators,” *J Appl Clin Med Phys*, vol. 16, no. 1, pp. 246–253, 2015, doi: 10.1120/jacmp.v16i1.5168.
- [27] C. Oare, C. Wilke, E. Ehler, D. Mathew, D. Sterling, and C. Ferreira, “Dose calibration of Gafchromic EBT3 film for Ir-192 brachytherapy source using 3D-printed PLA and ABS plastics,” *3D Print Med*, vol. 5, no. 1, 2019, doi: 10.1186/s41205-019-0040-4.
- [28] D. M. Kalaskar *et al.*, *3D Printing in Medicine*. 2017.
- [29] “How does Metal 3D printing work? | HP® Official Site.” <https://www.hp.com/us-en/printers/3d-printers/learning-center/how-does-metal-3d-printing-work.html> (accessed Jun. 26, 2023).
- [30] O. Semeniuk, A. Cherpak, and J. Robar, “Design and evaluation of 3D printable patient-specific applicators for gynecologic HDR brachytherapy,” *Med Phys*, vol. 48, no. 7, pp. 4053–4063, 2021, doi: 10.1002/mp.14888.

- [31] R. Sethi *et al.*, “Clinical applications of custom-made vaginal cylinders constructed using three-dimensional printing technology,” *J Contemp Brachytherapy*, vol. 8, no. 3, pp. 208–214, 2016, doi: 10.5114/jcb.2016.60679.
- [32] C. A. Bridger, M. J. J. Douglass, P. D. Reich, and A. M. C. Santos, “Evaluation of camera settings for photogrammetric reconstruction of humanoid phantoms for EBRT bolus and HDR surface brachytherapy applications,” *Phys Eng Sci Med*, vol. 44, no. 2, pp. 457–471, 2021, doi: 10.1007/s13246-021-00994-4.
- [33] L. B. Skinner, T. Niedermayr, N. Prionas, J. Perl, B. Fahimian, and E. A. Kidd, “Intensity modulated Ir-192 brachytherapy using high-Z 3D printed applicators,” *Phys Med Biol*, vol. 65, no. 15, 2020, doi: 10.1088/1361-6560/ab9b54.
- [34] L. B. Skinner, T. Niedermayr, N. Prionas, J. Perl, B. Fahimian, and E. A. Kidd, “Intensity modulated Ir-192 brachytherapy using high-Z 3D printed applicators,” *Phys Med Biol*, vol. 65, no. 15, 2020, doi: 10.1088/1361-6560/ab9b54.
- [35] A. Garg *et al.*, “An Algorithm for Computing Customized 3D Printed Implants with Curvature Constrained Channels for Enhancing Intracavitary Brachytherapy Radiation Delivery,” *2013 IEEE International Conference on Automation Science and Engineering (CASE)*, pp. 466–473, 2013, doi: 10.1109/CoASE.2013.6654002.
- [36] J. C. Lindegaard *et al.*, “Individualised 3D printed vaginal template for MRI guided brachytherapy in locally advanced cervical cancer,” *Radiotherapy and Oncology*, vol. 118, pp. 173–175, 2016, doi: 10.1016/j.radonc.2015.12.012.
- [37] S. Sekii *et al.*, “Inversely designed, 3D-printed personalized template-guided interstitial brachytherapy for vaginal tumors,” *J Contemp Brachytherapy*, vol. 10, no. 5, pp. 470–477, 2018, doi: 10.5114/jcb.2018.78832.
- [38] H. B. Z. Logar, R. Hudej, and B. Šegedin, “Development and assessment of 3D-printed individual applicators in gynecological MRI-guided brachytherapy,” *J Contemp Brachytherapy*, vol. 11, no. 2, pp. 128–136, 2019, doi: 10.5114/jcb.2019.84741.
- [39] “Brachy_Catalog_RAD10536A_September2019.pdf.” https://varian.widen.net/s/wwyx9dru1f/brachy_catalog_rad10536a_september2019 (accessed Aug. 24, 2023).
- [40] “A Biocompatible Polycarbonate 3D Printing Material.” <https://www.stratasys.com/en/materials/materials-catalog/fdm-materials/pc-iso/> (accessed Jun. 26, 2023).
- [41] “ABS-M30i: A Biocompatible Thermoplastic Material.” <https://www.stratasys.com/en/materials/materials-catalog/fdm-materials/abs-m30i/> (accessed Jun. 26, 2023).
- [42] “Biocompatible 3D Printing Materials.” <https://www.stratasys.com/en/materials/materials-catalog/polyjet-materials/biocompatible/> (accessed Jun. 26, 2023).
- [43] “Steam Sterilization | Disinfection & Sterilization Guidelines | Guidelines Library | Infection Control | CDC.” <https://www.cdc.gov/infectioncontrol/guidelines/disinfection/sterilization/steam.html> (accessed Jun. 26, 2023).
- [44] “Ethylene Oxide Sterilization | Disinfection & Sterilization Guidelines | Guidelines Library | Infection Control | CDC.” <https://www.cdc.gov/infectioncontrol/guidelines/disinfection/sterilization/ethylene-oxide.html> (accessed Jun. 26, 2023).

- [45] “Hydrogen Peroxide Gas Plasma | Disinfection & Sterilization Guidelines | Guidelines Library | Infection Control.”
<https://www.cdc.gov/infectioncontrol/guidelines/disinfection/sterilization/hydrogen-peroxide-gas.html> (accessed Jun. 26, 2023).
- [46] S. Bassi, B. Langan, and C. Malone, “Dosimetry assessment of patient-specific 3D printable materials for HDR surface brachytherapy,” *Physica Medica*, vol. 67, no. November, pp. 166–175, 2019, doi: 10.1016/j.ejmp.2019.10.035.
- [47] O. Pera *et al.*, “Validation of 3D printing materials for high dose-rate brachytherapy using ionisation chamber and custom phantom,” *Phys Med Biol*, vol. 66, no. 18, 2021, doi: 10.1088/1361-6560/ac226b.
- [48] I. Kawrakow, E. Mainegra-Hing, D. W. O. Rogers, F. Tessier, and B. R. B. Walters, “The EGSnrc Code System: Monte Carlo Simulation of Electron and Photon Transport,” 2023.
- [49] P. Andreo, “Monte Carlo simulations in radiotherapy dosimetry,” *Radiation Oncology*, vol. 13, no. 1, pp. 1–15, 2018, doi: 10.1186/s13014-018-1065-3.
- [50] M. J. P. Chamberland, R. E. P. Taylor, W. O. Rogers, and R. M. Thomson, “egs_brachy: a versatile and fast Monte Carlo code for brachytherapy,” *Physics in Medicine & Biology Phys. Med. Biol*, vol. 61, pp. 8214–8231, 2016, doi: 10.1088/0031-9155/61/23/8214.
- [51] P. Papaconstadopoulos, G. Hegyi, J. Seuntjens, and S. Devic, “A protocol for EBT3 radiochromic film dosimetry using reflection scanning,” *Med Phys*, vol. 41, no. 12, p. 122101, Dec. 2014, doi: 10.1118/1.4901308.
- [52] R. Ricotti *et al.*, “3D-printed applicators for high dose rate brachytherapy: Dosimetric assessment at different infill percentage,” *Physica Medica*, vol. 32, no. 12, pp. 1698–1706, 2016, doi: 10.1016/j.ejmp.2016.08.016.
- [53] L. Huang, H. Gaballa, and J. Chang, “Evaluating dosimetric accuracy of the 6 MV calibration on EBT3 film in the use of Ir-192 high dose rate brachytherapy,” *J Appl Clin Med Phys*, vol. 23, no. 5, 2022, doi: 10.1002/acm2.13571.
- [54] S. M. Glaser, H. Kim, and S. Beriwal, “Multichannel vaginal cylinder brachytherapy Impact of tumor thickness and location on dose to organs at risk”, doi: 10.1016/j.brachy.2015.08.009.
- [55] P. Trnková *et al.*, “Cervix cancer brachytherapy New inverse planning technology for image-guided cervical cancer brachytherapy: Description and evaluation within a clinical frame,” *Radiotherapy and Oncology*, vol. 93, pp. 331–340, 2009, doi: 10.1016/j.radonc.2009.10.004.
- [56] S.-J. Park, M. Chung, D. J. Demanes, R. Banerjee, M. Steinberg, and M. Kamrava, “Physics Contribution Dosimetric Comparison of 3-Dimensional Planning Techniques Using an Intravaginal Multichannel Balloon Applicator for High-Dose-Rate Gynecologic Brachytherapy”, doi: 10.1016/j.ijrobp.2013.08.008.